
Unterschrift Betreuer



TECHNISCHE
UNIVERSITÄT
WIEN
Vienna University of Technology

DIPLOMARBEIT

Utilising Elekta LINAC and MLC controller log files for phantom-less patient specific IMRT QA

ausgeführt am Atominstitut
der Technischen Universität Wien

unter der Anleitung von
Univ.-Prof. DI Dr. Dietmar Georg
und

DI Wolfgang Lechner, PhD
als verantwortlich mitwirkenden Universitätsassistenten

durch

Andreas Altendorfer, BSc

Hainburgerstraße 55/26,
1030 Wien

12. April 2017

Unterschrift Student

Acknowledgements

First of all, I would like to thank Univ.-Prof. DI Dr. Dietmar Georg for giving me the opportunity to carry out my MSc thesis at the Department for Radiation Oncology of the Medical University of Vienna. I gladly returned after a project work earlier in my studies, and once again experienced a highly professional as well as friendly working environment at the intersection of clinical routine and research.

My co-supervisor DI Wolfgang Lechner, PhD, not only took the time to answer all of my questions, but also encouraged me a lot.

Mag. Barbara Knäusl, PhD, and Mag. Peter Kuess, PhD, did a perfect job in organising and leading the students meetings and the seminar, where I could gain know-how in presenting my work to others.

Of course, this study would not have been possible without the software developed by my dear colleague Andreas Moser.

Above all, I am deeply grateful to my mother for her great support throughout my years of study.

Abstract

Introduction: Intensity-modulated radiation therapy (IMRT) is the state of the art treatment technique in external beam radiotherapy. Currently, quality assurance (QA) procedures rely mostly on phantom-based experimental measurements. However, electronic log files, which originate from the linear accelerator (LINAC) or multi leaf collimator (MLC) controller, offer promising novel options for QA. Using this methodology, a variety of machine parameters can be recorded during the treatment. The aim of this MSc thesis was to explore and validate this log file-based QA.

Materials and Methods: Two different models of LINACs, Versa HD and Synergy (Elekta AB, Stockholm, Sweden), were used to perform three test plans on a weekly basis: a 4-field-box, a head & neck volumetric-modulated arc therapy (VMAT) as well as a static picket fence (PF) test. The study duration was six months. XML type log files (MLC leaf positions, electric gun current etc.) were acquired during every irradiation using the option service graphing of the machine's service mode. An in-house software was applied to evaluate deviations of the leaf positions from the test plan (as defined in the DICOM file). A mean leaf positioning error was calculated as the average of a mean measurement bank error over all measurements. The integrated electronic portal imaging device (EPID) and a detector array (Delta⁴, ScandiDos AB, Uppsala, Sweden) provided reference data. The sensitivity of all measurement methods was analysed by means of implementing leaf errors in the static and also dynamic PF test plan.

Results: For the static plans (PF test, 4-field-box), Versa HD log files showed a lower mean leaf positioning error (0.010 mm X1/ -0.002 mm X2, 0.002 mm X1/ -0.042 mm X2) compared to the Synergy (-0.301 mm/ 0.309 mm, -0.296 mm/ 0.291 mm). The EPID obtained higher values for the standard deviation than the log files, which could be attributed to the finite resolution of the EPID panel (pixel size of 0.4 mm). Interestingly, no agreement in the time development of the mean measurement bank error could be observed between log file and EPID data (Pearson correlation coefficient around 0.3; even smaller values were obtained

between log files and Delta⁴ VMAT measurements: 0.06). Implemented leaf errors of 0.5, 1 and 2 mm could be detected by the EPID as well as the log files. A rather small but significant influence of gravity was noticed by the log file analysis on the Versa HD. The gun current declined by 0.08 mA on Versa HD and 0.22 mA on Elekta Synergy, respectively.

Discussion/Conclusion: Log files appear to be able to provide a variety of useful data for every treatment delivery performed, e.g. influence of gravity, decrease in gun current. Although the log files did not reflect the time behaviour monitored by the EPID and the Delta⁴ phantom on a long-time basis, it was possible to detect artificially introduced leaf errors. The simultaneous use of an independent system monitoring the leaf calibration is indicated. Once generally available on Elekta machines, log files might have the potential to act as an additional QA procedure.

Zusammenfassung

Einleitung: Die Intensitätsmodulierte Strahlentherapie (IMRT) stellt den Stand der Technik in der Strahlen-Teletherapie dar. Die Qualitätssicherung (QS) stützt sich dabei momentan hauptsächlich auf externe phantom-basierte Messungen. Eine vielversprechende neue Methode zeichnet sich in der Verwendung elektronischer Log-Files des LINAC (Linearbeschleuniger)- bzw. MLC (Multilamellenkollimator)-Controllers ab. Diese Technologie ermöglicht die Aufnahme einer Vielzahl von Maschinenparametern während der Bestrahlung. Das Ziel dieser Masterarbeit war es, Log-Files als potentiell Instrument in der QS zu validieren.

Materialien und Methoden: Auf zwei unterschiedlichen LINACs, Versa HD und Synergy (Elekta AB, Stockholm, Schweden), wurden wöchentlich drei Testpläne abgestrahlt: Eine 4-Felder-Box, eine HNO Volumetric Modulated Arc Therapy (VMAT) und ein statischer Picket-Fence (PF) Test. Die Studiendauer betrug 6 Monate. Die Abstrahlungen fanden im Service-Modus der Maschinen statt. Mittels der Option „Service-Graphing“ wurden Log-Files als XML-Dateien generiert. So konnten unter anderem die Lamellenpositionen und der Strom über die Elektronenkanone aufgezeichnet werden. Eine hausintern entwickelte Software ermöglichte nun die Bestimmung der Abweichungen der Lamellenpositionen von den Planwerten (aus den DICOM-Dateien). Als Maß für die erzielte Positionierungsgenauigkeit der MLC-Bank eines LINACs wurde der Mean Leaf Positioning Error eingeführt und berechnet. Er stellt einen arithmetischen Mittelwert (des Mean Measurement Bank Errors) über alle durchgeführten Messungen eines Testplans dar. Das integrierte Electronic Portal Imaging Device (EPID) als auch ein Detektorarray (Delta⁴, ScandiDos AB, Uppsala, Schweden) lieferten Referenzdaten. Um die Sensitivität der unterschiedlichen Messmethoden zu ermitteln, wurden im statischen (und auch dynamischen) PF-Test einzelne Lamellen manipuliert.

Ergebnisse: Laut den Log-File Daten erzielte Versa HD bei den Testplänen mit statischen Feldern (PF-Test, 4-Felder-Box) einen niedrigeren Mean Leaf Positioning Error (0,010 mm X1/ -0,002 mm X2, 0,002 mm X1/ -0,042 mm X2) als das Synergy Modell (-0,301 mm/ 0,309 mm, -0,296 mm/ 0,291 mm). Das EPID zeigte

höhere Standardabweichungen als die Log-Files, vermutlich aufgrund der endlichen Auflösung des Panels mit einer Pixelgröße von 0,4 mm. Interessanterweise konnte keine Übereinstimmung der zeitlichen Entwicklung des Mean Measurement Bank Errors, ermittelt über Log-Files und EPID, gefunden werden (Pearson-Korrelationskoeffizient $\sim 0,3$; zwischen Log-Files und Delta⁴-VMAT Messungen sogar nur 0,06). Am Versa HD konnten die Log-Files einen Einfluss der Gravitation auf die Lamellen feststellen. Der Gun-Strom nahm im Untersuchungszeitraum um 0,08 mA (Versa HD) bzw. 0,22 mA (Synergy) ab.

Diskussion/Fazit: Log-Files ermöglichen es, bei jeder Bestrahlung eine Vielzahl von Maschinendaten aufzuzeichnen. In dieser Arbeit konnten daraus z. B. ein Einfluss der Gravitation auf die Lamellen und die Abnahme des Stromes über die Elektronenkanone sicht- und überwachbar gemacht werden. Zwar konnten die Log-Files die zeitliche Entwicklung des Systems, gemessen durch das EPID und das Delta⁴-Phantom, nicht bestätigen, künstlich eingeführte Lamellenfehler wurden jedoch detektiert. Es ist anzuraten, parallel eine unabhängige Überwachung der Lamellen-Kalibrierung durchzuführen. Unter dieser Voraussetzung könnten Log-Files eine zusätzliche Maßnahme im Rahmen der QS darstellen.

Contents

1	Introduction	1
1.1	Radiation therapy	1
1.2	Physics, chemistry and biology	2
1.3	Linear accelerator and treatment delivery	6
1.3.1	Electron gun	8
1.3.2	Magnetron, klystron	8
1.3.3	Accelerator tube	10
1.3.4	Treatment head and multi leaf collimator	10
1.3.5	Calibration and absolute dosimetry	12
1.3.6	Treatment delivery modalities	14
1.3.7	Treatment planning and dose calculation	15
1.4	Advanced external beam radiotherapy devices	17
1.5	Quality assurance	18
1.6	Literature	20
1.7	Purpose and aim	25
2	Materials and Methods	28
2.1	LINACs	28
2.1.1	Versa HD (Agility) - additional specifications	29
2.1.2	Operation	29
2.2	Delta ⁴ phantom and gamma index	29
2.3	Log files and in-house software	32
2.4	Static picket fence test	34
2.5	Consistency checks	36
2.6	Additional tests	37
2.6.1	Dynamic PF test	37
2.6.2	Analysis of the influence of gravity	38
2.7	Sensitivity analysis	38
2.8	Data analysis - leaf error definitions	41

3	Results	43
3.1	Static PF test, consistency checks	43
3.1.1	Mean leaf positioning error	43
3.1.2	Mean measurement bank error	45
3.1.3	Mean leaf positioning error (absolute)	45
3.1.4	Mean measurement leaf error	52
3.2	Additional tests	52
3.2.1	Dynamic PF test	52
3.2.2	Analysis of the influence of gravity	58
3.3	Sensitivity analysis	61
3.4	Gun current	69
4	Discussion	72
4.1	Static PF test, consistency checks	72
4.2	Additional tests	74
4.2.1	Dynamic PF test	74
4.2.2	Analysis of the influence of gravity	75
4.3	Sensitivity analysis	76
4.4	Gun current	77
5	Conclusions	78
	Acronyms	79
	List of Figures	81
	List of Tables	83
	References	84

1 Introduction

1.1 Radiation therapy

In radiation therapy, cancer is treated by means of ionising radiation ($>10 \text{ eV}^1$), such as X-rays or particle beams. Two approaches are common:

- brachytherapy
- teletherapy (external beam radiation therapy)

Brachytherapy is a method where (sealed) radioactive sources (radioisotopes), e.g. ^{60}Co , ^{137}Cs , ^{192}Ir [2], are brought directly to the malign tissue. This is usually done by means of a so-called afterloading machine. Applicators (made of plastic or metal) are attached to a cancer-affected body cavity (intracavitary brachytherapy), for example oesophagus or vagina [3]. The source, sealed in a stainless steel shell, is automatically moved from the shielded safe in the machine to the applicator through a guide tube (loading). γ radiation will be set free until unloading. Also an implantation of applicator and source is possible (interstitial brachytherapy), for example in prostate or tongue [3]. In a typical radiotherapy department, about 10-20% of all radiotherapy patients are treated with brachytherapy [2].

By comparison, in teletherapy, the radiation source is located at the outside of the patient. Historically, also radioisotopes (^{60}Co) alongside X-ray tubes were used. Nowadays, the medical linear accelerator (LINAC) is the state of the art device. The patient is positioned on a treatment couch with an MV X-ray source (gantry) being able to irradiate from various angles. This machine will be described in detail in Sec. 1.3 as it represents the subject of this study.

Either way, the radiation hits the tumour, which then absorbs its energy. The absorbed dose D (Gy) is given by

$$D = \frac{dE_{abs}}{dm} \quad (1)$$

1 Gy = 1 J of absorbed energy E_{abs} per kg absorber mass m . Typically, radiation therapy is performed in fractions. A standard scheme is given by a daily application

¹ An energy of 15 eV is required to extract one electron from a molecule of a biological material [1].

of around 2 Gy, mostly with 5 fractions per week, until 60 Gy are reached after 6 weeks [4]. In so doing, tumour cells are harmed, preferably through double-strand breaks of the deoxyribonucleic acid (DNA), stored in the cell nucleus. It is always tried to prevent surrounding tissue and so-called organs at risk (OAR) from damage. Beam directions and shapes (fields) are planned on this premise.

Radiation therapy is either solely applied (cancer in adenoid tissue, testis, cerebellum [4]) or part of a mixture of cancer therapies amongst surgery (pre- or postoperative) and chemotherapy. Besides curative radiation therapies, also a palliative goal, e.g. pain treatment, can be pursued in bad cases.² Moreover, benign diseases can be treated as well with radiation.

1.2 Physics, chemistry and biology

This section is based on the textbooks by Mayles et al. [1] and Khan [6] (physics) as well as Wannemacher et al. [4] (chemistry and biology).

Physical interaction between radiation and matter depends on the type of radiation as well as on its energy spectrum. For X-rays (100 eV to 100 keV) and γ radiation (>100 keV), respectively, the observed effects are:

- interaction with electrons of the atomic shell
 - elastic scattering
 - photoelectric effect
 - inelastic scattering (Compton effect)
- interaction with the atomic nucleus' Coulomb (electrostatic) field
 - pair production
- interaction with the atomic nucleus
 - photonuclear reaction

In radiology (clinical diagnostics) and radiation therapy, photoelectric effect, Compton effect and pair production are most important. For this reason, they will be explained in the following paragraphs.

² 55% of all (treated) cancer patients receive “palliation” [5]

A photon with the energy $h \cdot \nu$ exceeding the binding energy E_b of an electron has the ability to knock it out of the atomic shell. The photon is absorbed, and the electron is provided the kinetic energy

$$E_{kin} = h \cdot \nu - E_b \quad (2)$$

This is called the **photoelectric effect**. The secondary electron (photoelectron) itself has got the ability to ionise atoms. In addition, the hole that is left in the particular electron shell will be filled by an electron of a higher shell (difference in binding energy!) under the emission of electromagnetic dipole radiation, i. e. characteristic X-rays. The competing process of energy emission is given by the radiation-less Auger effect, where an outer shell electron is ejected instead.

The **Compton effect** represents the interaction of a photon with a “free” (weakly bound) electron that is considered to be at rest. In other words, the momentum transferred to the electron greatly exceeds the momentum of the electron in the bound state. The inelastic scattered photon leaves with an energy

$$E' = \frac{E}{1 + \frac{E}{m_0 \cdot c^2}(1 - \cos \theta)} \quad (3)$$

$E = h \cdot \nu$ denotes the photon’s primary energy, $m_0 \cdot c^2$ the electron’s rest energy (511 keV) and θ the scattering angle. The energy of the electron after scattering is given by

$$E_e = E - E' \quad (4)$$

Thus the energy loss of the photon, which results in an increased wavelength³.

If a photon enters the Coulomb field of a nucleus, the **production of an electron-positron pair** becomes possible. The positron is the electron’s antiparticle. They differ only in the algebraic sign of their charges (electron: $-e_0$, positron: $+e_0$). The sum of their rest masses equals 1,022 keV. Hence a photon energy of at least this numerical value is necessary for a pair production. Excess energy ($h \cdot \nu - 2 \cdot m_0 \cdot c^2$) results in kinetic energy of the particles, which may have the ability to ionise atoms. The positron is likely to annihilate with an electron

³ The increase in wavelength for a given θ is characteristic for the scattered particle \rightarrow Compton wavelength

under the emission of two photons (γ radiation) with 511 keV kinetic energy each.

Overall, the attenuation of a photon beam travelling through matter can be described by Beer-Lambert's law

$$I(x) = I_0 \cdot e^{-\mu \cdot x} = I_0 \cdot e^{-\mu_m \cdot \rho \cdot x} \quad (5)$$

The intensity I (W/cm^2) decreases exponentially with penetration x (cm) from a primary intensity I_0 present at the surface. On a side note, the formula holds for one particular wavelength only. $\mu = \mu(E)$ is the so-called linear absorption coefficient ($1/\text{cm}$). It incorporates the photoelectric effect (τ), Compton effect (σ) as well as pair production (χ).

$$\mu = \tau + \sigma + \chi \quad (6)$$

μ_m is the mass absorption coefficient, given by μ divided by the density ρ (g/cm^3) of the absorber. The following formulas show the dependencies of the particular mass absorption coefficients on the atomic number Z of the absorber and the photon beam energy E .

$$\tau_m \propto \frac{Z^3}{E^3} \quad (7)$$

$$\sigma_m \propto Z \quad (8)$$

$$\chi_m \propto Z \cdot \ln E \quad (9)$$

The human body has a Z of about 8 to 12, varying with age (bone density). In radiology, the photon energies range from 20 to 120 keV [7], in radiation therapy from 1 to 25 MeV. As depicted in Fig. 1, the Compton effect is dominating in these energy zones. On the lower energy side, photoelectric effect and on the higher energy side, pair production also play a role.

Biomolecules can be affected by radiation either directly or indirectly. If absorption of radiation and excitation/ionisation coincide, **direct radiation effects** are present. However, by means of production of chemical reactive molecules (radicals) and their diffusion, **indirect (secondary) radiation effects** on distant

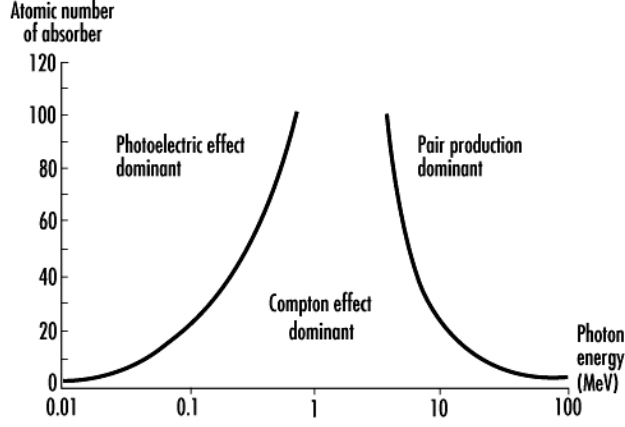
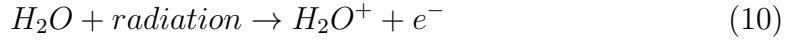


Figure 1: Relative importance of the three principal interactions of photon beams in matter: The two curves represent $\tau = \sigma$ and $\sigma = \chi$, respectively [8].

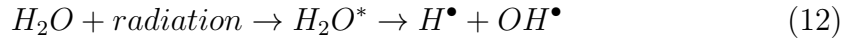
biomolecules are possible. For the most part, water is the medium responsible for indirect effects due to its high share in biological substances. One chain of reactions is given by the separation of an electron



for which an energy of 12.56 eV is necessary. Next the H_2O^+ ion dissociates

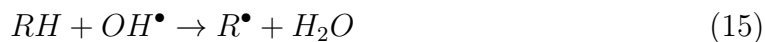


with OH^\bullet being a radical. The separated electron is also able to cause radicals. Another possibility is represented by



i. e. excitation of the water molecule and subsequent dissociation into radicals. Eventually, the water radicals will react with/harm biomolecules RH . For example

through



As already mentioned, the biomolecule targeted in radiation therapy is the DNA of the malign tissue, which bears the genetic information, e. g. needed for protein synthesis. It consists of deoxyribose (a sugar), phosphate as well as nitrogen-containing bases: cytosine, thymine, adenine and guanine. Base pairs can be built by:

- cytosine & guanine
- thymine & adenine

via hydrogen bonds. These pairs connect the two single strands of sugars and phosphates to a double-strand, which, in addition, is coiled, resulting in a double helix (see Fig. 2). Around 1 m of DNA is contained in every human cell nucleus.

However, damage to the DNA is done by liberation of bases as well as strand breaks and is mostly caused by direct radiation effects. Indeed, the body offers repair mechanisms⁴, but they are weak concerning double-strand breaks. Ultimately, radiation will cause a dysfunction of the malign cells, inhibit proliferation and lead to cell death.

1.3 Linear accelerator and treatment delivery

This section is based on the book “The physics of radiation therapy” by Khan [6].

The LINAC represents the most commonly applied device in modern external beam radiation therapy. It uses high-frequency electromagnetic waves to accelerate charged particles such as electrons to high energies through a linear tube [6]. Treating superficial tumours, the electron beam itself is used, whereas deep-seated

⁴ which can be inhibited by administration of chemotherapeutics → chemo-radiotherapy

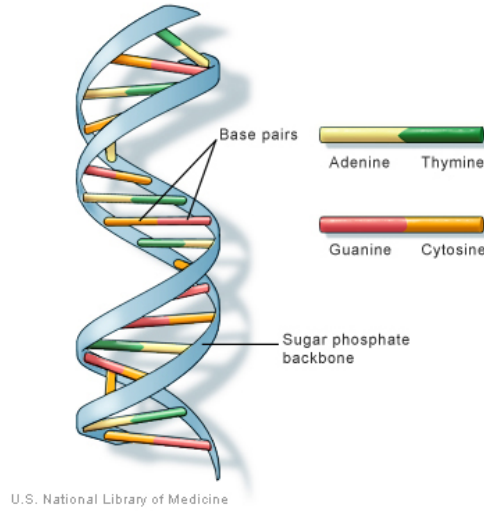


Figure 2: Deoxyribonucleic acid (DNA) double helix [9].

tumours are irradiated by X-rays, produced when the electron beam hits a target. Typically, the energy of the electron beam lies between 6 and 20 MeV (unusually up to 30 MeV). The nominal photon beam energy typically ranges from 4 to 25 MeV (with a maximum of 50 MeV). Generally, a dose rate⁵ of about 6 Gy/min can be achieved. In the special case of flattening filter free beams (FFF), up to 24 Gy/min are possible.

Figure 13 in Sec. 2.1 shows an Elekta Synergy as well as a Versa HD LINAC. Or rather, the machines' parts that are located in the treatment room, such as the adjustable treatment couch and the gantry, which is able to rotate around the patient by 360°. A block diagram of a typical medical LINAC is depicted in Fig. 3. Accordingly, an **electron gun** emits electrons. At the same time, microwaves are produced by a **magnetron or klystron**. The electrons as well as the microwaves are then injected into the **accelerator tube** (contained in the gantry) by means of a modulator in order to synchronise them. Two concepts for accelerating the electrons are common: accelerating via a travelling or stationary wave. The tube's design depends on the selected method. The electrons are brought almost to the speed of light by Coulomb force, resulting from the microwave's⁶ axial vector

⁵ $\dot{D} = \frac{dD}{dt}$

⁶ transverse magnetic waves are used: TM010 ($H_z = 0$)

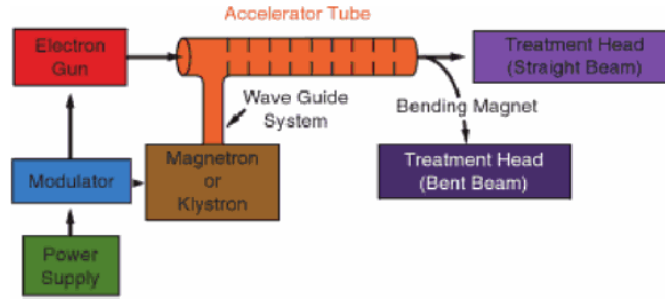


Figure 3: Block diagram of a typical medical linear accelerator (LINAC) [6].

component of the electric field strength E_z . After that, they leave the tube as a pencil beam of about 3 mm in diameter. Usually, the beam is bent using magnets to reach the **treatment head**.

1.3.1 Electron gun

Similar to an X-ray tube, electrons are extracted from a thermal electron source in most cases, either a directly heated tungsten filament or a non-directly heated tungsten matrix (hot cathodes). Alternatively, a grid cathode (cold cathode) can be applied. It is coated with barium sulphate, for instance, which lowers the electrons' work function so that an adequate voltage relative to the anode is sufficient to extract them without the need of heating.

A modulator electrode focuses the electron beam, in other words, minimises the angle of beam spread via a negative electric potential.

The anode is made as a hollow anode so that the electron beam is able to leave the gun.

1.3.2 Magnetron, klystron

The acceleration unit needs to be fed with high-frequency microwaves of about 3 GHz (radar). The microwave production is either achieved by using a magnetron or a klystron.

Figure 4 shows the sectional view of a magnetron, which is a cylindrical construction. It consists of a rotor, representing the cathode (hot cathode), and a stator, working as the anode, which contains cavities. Both are usually made of

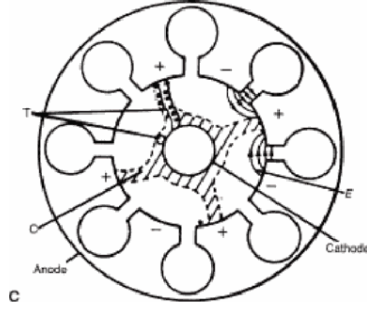


Figure 4: Magnetron, sectional view [6].

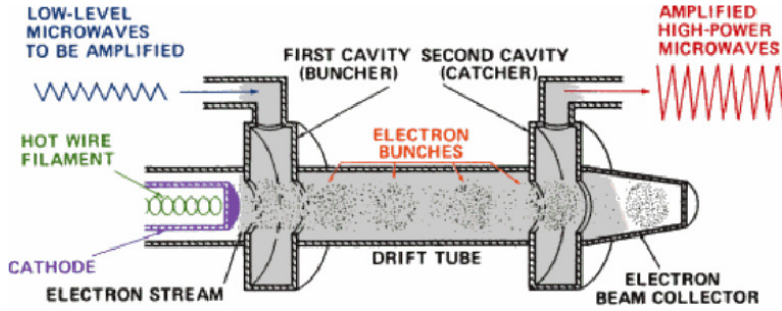


Figure 5: Two-cavity klystron [6].

copper. In addition to the pulsed direct current electric field between these parts, a static magnetic field is applied perpendicular, i.e. in axial direction. For that reason, the electrons emitted from the cathode move towards the anode in spirals, radiating energy in the form of microwaves. These are coupled out of the cavities via a waveguide system.

LINACs with a higher energy rather use a klystron. In comparison to the magnetron, it is not a generator of microwaves but a microwave amplifier, which needs to be driven by a low-power microwave oscillator. There are basically two types, namely the multicavity klystron (two or more cavities) and the reflex klystron (one cavity). The former is shown in Fig. 5. Two cavities are located between the cathode and the anode. The emitted electrons are accelerated by a pulse of voltage into the first cavity (buncher cavity), which is fed with a low-power microwave. As a result, the electrons get speeded up or slowed down (velocity modulation) and form bunches. As these bunches enter the second cavity (catcher cavity), after passing a drift tube, they induce a microwave of a higher power.

1.3.3 Accelerator tube

For the use of a travelling wave, the accelerator tube is made of metal so as to provide an adequate propagation of the electromagnetic wave (high reflectance of metal). The length depends on the energy intended, typically 0.5 to 2.5 m. The microwaves are injected into one end and travel along the evacuated tube until they reach the opposite side, where they are absorbed by means of a terminating load in order to prevent a backward reflection. Since the electrons are much slower than speed of light when injected, for example $v_e = c/2$, the wave's phase velocity v_p is decreased by using iris-apertures in order to ensure the so-called matching condition $v_p \approx v_e$ that is necessary for the process. Consequently, such a construction is called an iris-loaded waveguide.

However, the electrons are pulled along by the travelling wave, located on the positive falling edge, like a surfer (compare Fig. 6), building bunches that exit the tube in radar frequency.⁷ In addition, the beam is pulsed by about 100 to 400 Hz due to power supply reasons.

By contrast, if a standing wave should be applied, the tube's length is chosen in such a way that the microwaves with an intended frequency are reflected and are able to build the standing wave. Obviously, a terminating load is missing. The microwaves are coupled into the side structure via side coupling cavities. The electrons are accelerated throughout the whole flight, except when passing nodal points, because the cavities reverse their polarity in an adequate manner (see Fig. 7).

1.3.4 Treatment head and multi leaf collimator

The treatment head (Fig. 8) is made of shielding material, such as lead, tungsten or lead-tungsten alloy. It contains an X-ray target, scattering foil, flattening filter, ion chamber, fixed and movable collimator and light localizer system [6]. Some parts are used for photon treatments only, while others are used for electron treatments.

For photon treatments, similarly to an X-ray tube, the target is made of high Z materials like tungsten, because bremsstrahlung increases with Z^2 while energy

⁷ $W = e_0 \int_0^l E_z(z) \sin \varphi(z) dz \dots$ electron energy with $\varphi = \omega t - k_g z \dots$ phase

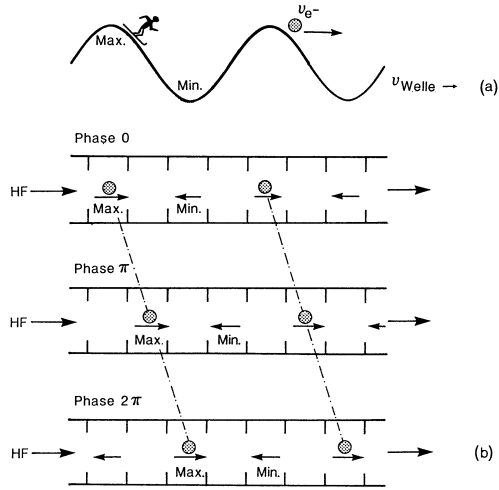


Figure 6: Concept of electron acceleration via a travelling wave [10].

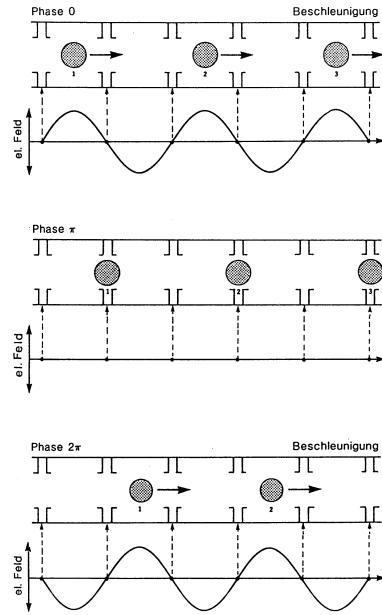


Figure 7: Concept of electron acceleration via a standing wave [10].

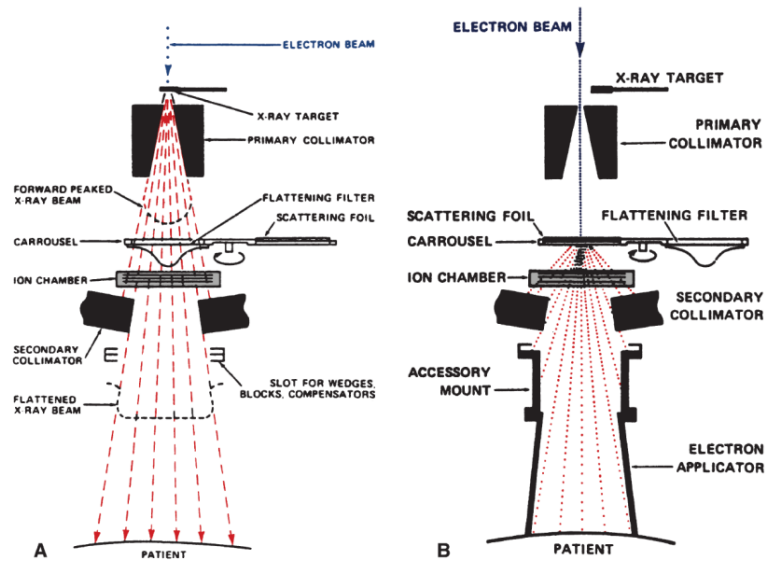


Figure 8: Treatment head of medical LINAC, schematic: photon mode (A), electron mode (B) [6].

loss from collision only with Z .

The flattening filter is made of steel, brass or lead. It has the ability to flatten the raw beam and to make it uniform across the field. This has to be done due to the angular distribution of the X-rays produced, which is strongly forward peaked (the higher the energy, the higher the peak). To be precise, the flattening filter attenuates the centre of the raw beam to levels equal to the periphery (due to its conical shape). However, there is a tendency towards FFF beams. Advantages are the increased dose rate (and therefore shorter treatment time) and the reduced scatter- and leakage radiation [11]. Furthermore, it is not necessary to check the mechanical position of the flattening filter for angular and positional errors in quality assurance.

For electron treatments, the pencil beam leaving the tube hits a scattering foil so as to broaden the beam and provide a uniform electron fluence⁸ ($1/\text{m}^2$) across the treatment field. The scattering foil is a thin metallic foil, made of lead, sometimes used in combination with a second foil, made of aluminium.

At first, the treatment beam is collimated by a fixed primary collimator. It defines the largest possible circular field. Then the beam passes two transmission ion chambers for dose monitoring (\Rightarrow monitor units (MUs)). On a side note, two units are applied on patient safety grounds. After that, it is further collimated by moveable collimators (X -/ Y -jaws). A light localising system is installed for the possibility to check the configured field size.

Nowadays, multi leaf collimators (MLCs) (see Fig. 9) are state of the art for the ultimate collimation of the X-ray beam. They contain two opposed banks of parallel tungsten leaves, with up to 80 leaves each. They are controlled by the computer and moved automatically to form mostly every irregular tumour shape (or rather target volume shape) according to its cross section.

1.3.5 Calibration and absolute dosimetry

This subsection is based on the handbook by Podgorsak [2].

Before clinical use, the output of photon and electron beams produced by external beam radiotherapy machines must be calibrated [2]. The calibration represents

⁸ $\Phi = \int_{t_1}^{t_2} \varphi dt$ with $\varphi = \frac{d^2 N}{dA dt} \dots$ flux density ($1/\text{m}^2\text{s}$)

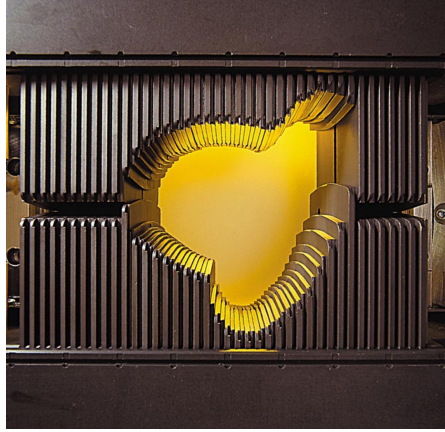


Figure 9: Multi leaf collimator (MLC) by Varian Medical Systems Inc. (Palo Alto, U.S.) [12].

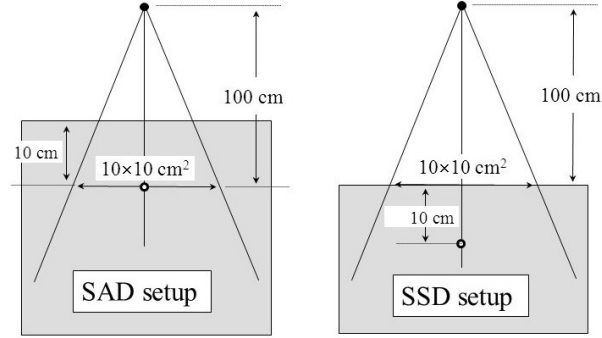


Figure 10: Source to axis distance (SAD) vs. source to surface distance (SSD) setup for photon beam calibration; edited from [13].

the first important step to an accurate dose delivery. The basic output is usually stated as the dose rate for a point P at a reference depth z_{ref} (often the depth of dose maximum z_{max}) in a water phantom for a nominal source to surface distance (SSD) or source to axis distance (SAD) and a reference field size (often $10 \times 10 \text{ cm}^2$) on the phantom surface or the isocentre [2]. The output is given in Gy/MU. For an SAD setup, 100 MU represent an absorbed dose of 1 Gy (or $1 \text{ MU} \hat{=} 1 \text{ cGy}$), delivered to point P at $SAD = 100 \text{ cm}$ and $z_{ref} = 10 \text{ cm}$. Figure 10 illustrates these reference conditions.

The measurement of the dose rate is usually done via an ionisation chamber.

The ion chamber has a sensitive volume of around 0.1 to 1 cm³, usually filled with ambient air. Ionising radiation will produce electrons and ions, i. e. electric charges Q . Charge and air mass m_{air} are related to absorbed dose in air D_{air} by

$$D_{air} = \frac{Q}{m_{air}} \left(\frac{W_{air}}{e} \right) \quad (17)$$

where (W_{air}/e) is the mean energy required to produce an ion pair per unit charge (the current value for dry air is 33.97 eV/ion pair or 33.97 J/C) [2]. Subsequently, a conversion of the absorbed dose in air to the dose to the medium (water) has to be made.

In clinical practice, calibration protocols are used for the conversion of ionisation to dose, e. g. IAEA TRS-389 [14]: the absorbed dose to water at the reference depth z_{ref} in water, in a photon beam of quality Q and in the absence of the chamber, is given by

$$D_{w,Q} = M_Q N_{D,w,Q_0} k_{Q,Q_0} \quad (18)$$

where M_Q is the reading of the dosimeter with the reference point of the chamber positioned at z_{ref} in accordance with the reference conditions and corrected for the influence quantities temperature and pressure, electrometer calibration, polarity effect and ion recombination. N_{D,w,Q_0} is the calibration factor in terms of absorbed dose to water for the dosimeter at the reference quality Q_0 , and k_{Q,Q_0} is a chamber specific factor which corrects for the difference between the reference beam quality Q_0 and the actual quality being used, Q [14].

1.3.6 Treatment delivery modalities

Historically, the kilovoltage X-ray treatment beam could only be delivered from one fixed angle. Later, the megavoltage γ radiation of a cobalt-60 machine or a LINAC could be varied in its direction. Target specific beam shapes were achieved by the fabrication of cast blocks which were used as secondary collimators of the rectangular field (not completely outdated yet). This can be referred to as **conventional radiation therapy**. The development of computed tomography (CT) and thus gathering three-dimensional information of the anatomical region

of interest (ROI)⁹ facilitated **3D conformal radiation therapy (CRT)**. Using many fields as well as gantry angles, a more conformal irradiation of the target volume had become possible.

The invention of the MLC spared the need of manually changing blocks. The LINAC's gantry can be rotated to a certain position where the adequate field is automatically loaded (also consecutive irradiations of different segments from one gantry angle are possible). This is called **step & shoot** and represents the first modality of an **intensity-modulated radiation therapy (IMRT)**. On a side note, although it is called an intensity-modulation, rather the fluence is modulated since only the beam shape (area) is adjusted via the MLC. The second modality is called **Dynamic MLC** in which the positions of the leaves are adjusted during the irradiation process. However, still happening at a certain gantry angle. The next step was only logical. It has been named **intensity-modulated arc therapy (IMAT)** as the gantry is able to rotate during the beam delivery, i. e. describes an arc, with simultaneous leaf movements and dose rate variations. In Elekta's product range, this modality is called **volumetric-modulated arc therapy (VMAT)**. In comparison to IMRT, in VMAT also the dose rate, i. e. intensity, is varied.

1.3.7 Treatment planning and dose calculation

A prerequisite for meaningful 3D treatment planning and for accurate dose reporting is the volume definition [2]. The latest recommendations contain:

- gross tumour volume (GTV)
- clinical target volume (CTV)
- internal target volume (ITV)
- planning target volume (PTV)

The **GTV** is the gross palpable or visible/demonstrable extent and location of malignant growth [2]. It is based on clinical examination and on the use of imaging

⁹ not only are images used in a visual way, but also the numerical information about the electron density is processed in treatment planning

modalities, such as CT and magnetic resonance imaging (MRI). The **CTV** is the tissue volume that contains a demonstrable GTV and/or sub-clinical microscopic malignant disease, which has to be eliminated [2]. Selection and delineation of GTV, CTV as well as OAR is based on the anatomy or physiology of the patient and therefore arises from a medical decision. The **ITV** consists of the CTV plus an internal margin. The internal margin is designed to take into account the variations in the size and position of the CTV relative to the patient's reference frame [2]. In other words, organ motions or variations in bladder and rectal content are incorporated. The **PTV** is a geometrical concept, and it is defined to select appropriate beam arrangements, taking into consideration the net effect of all possible geometrical variations, in order to ensure that the prescribed dose is actually delivered to the CTV [2]. To put it in another way, the PTV includes external margins, which consider the patient set-up and the beam alignment. ITV and PTV can be constructed automatically as 3D models by the treatment planning system (TPS).

Apart from the volumes that have to be considered, the complete prescription of a radiotherapy treatment must include the definition of the aim of the therapy and the prescription of dose and fractionation. The patient dimensions are required for the calculation of treatment time and MUs, respectively. Bony or fiducial marks work as landmarks to match the positions in the treatment plan with the positions on the patient. For a 3D treatment planning, a CT data set of the ROI is necessary. An external contour (representative of the skin or immobilization mask) must be drawn on every CT slice. The tumour and treated volume are usually drawn on CT slices by the radiation oncologist [2]. OARs and other important structures should also be delineated.

In the course of the treatment planning, the delivery will be simulated, commonly on a special treatment simulator machine. This machine offers the same geometry as the LINAC, but is equipped with a kV X-ray source instead. For this reason, an acquisition of radiographs (or fluoroscopy) through the planned treatment beam directions becomes possible. The treatment simulation also enables [2]:

- determination of the patient treatment position
- identification of the target volumes and OARs

- determination and verification of the treatment field geometry
- acquisition of patient data for treatment planning

The dose calculation itself is computerised and done using a TPS. Of course, beam and patient data are the starting point for the calculation. The most critical software component is the dose calculation algorithm. It has to take into account the complexity of radiation interactions (physical models) with the human tissues and has to predict the dose delivered to any point within the patient. Available algorithms are, for instance, the pencil beam, convolution-superposition and Monte Carlo simulation. Usually, they are based on a publication, but stay hidden in the software, because of proprietary reasons.

After the dose calculations are performed, a radiation oncologist evaluates the plan. The following tools are used to do so:

- isodose curves
- orthogonal planes and isodose surfaces
- dose distribution statistics (for example minimum, maximum or mean dose to a certain volume)
- differential dose-volume-histograms (DVHs)
- cumulative DVHs

1.4 Advanced external beam radiotherapy devices

Accuracy Inc. (Sunnyvale, U.S.) offers advanced external beam radiotherapy devices using X-rays, namely CyberKnife and TomoTherapy. They were originally developed at Stanford University and University of Wisconsin-Madison, respectively.

The CyberKnife (Fig. 11, left) is a compact 6 MeV LINAC attached to an industrial robot with six axes. This construction enables a beam delivery from any angle. A fixed tungsten collimator of a certain diameter creates a circular field. Two X-ray tubes and imagers produce a stereoscopic image that is necessary for locating the target volume and allows for patient movement. In other words, the deviation



CyberKnife [17]



TomoTherapy [18]

Figure 11: Advanced external beam radiotherapy devices by Accuray.

of the target from the planned position is tracked, and the beam directions are automatically corrected in order to adjust for the shift [15]. The CyberKnife System is used to deliver a stereotactic radiosurgery (SRS)/stereotactic body radiation therapy (SBRT) with sub-millimeter accuracy [16].

TomoTherapy (Fig. 11, right) utilises a CT-scanner platform in which also a small 6 MeV LINAC is integrated. The keV as well as the MeV source is able to rotate around the patient. It is the only radiation system specifically designed for integrated, 3D image-guided radiation therapy (IGRT)¹⁰ [16]. The TomoTherapy system features an MLC and IMRT. The delivery is either performed slice by slice (discrete movement of the couch) or helically (continuous movement).

1.5 Quality assurance

Quality can be defined as fulfilling the customers' expectations [19]. In contrast to articles of daily use, the customer, i. e. patient, will not be satisfied with fitness for use. He will demand a treatment of highest quality.

Modern quality management (QM) is to be understood as the entirety of all quality-related actions and aims [20]. Continuous improvement of processes is an integral part in it. Regarding a continuous improvement process (CIP), a university hospital should benefit from its scientific findings as well as early adoptions.

¹⁰ IGRT takes into account the inaccuracy of patient positioning and anatomical changes between fractionated deliveries by means of pre-treatment imaging.

In quality assurance (QA) for medical treatments, especially radiation applications, one quality demand coming from the public (legislator) is very important: safety of life or physical condition. Apart from a possible healing, the treatment should not harm the patient (nor the staff \Rightarrow radiation protection). Even though physician and patient may decide to take a risk.

QA in external beam radiotherapy should incorporate all processes in the treatment chain. It reduces uncertainties and errors in dosimetry, treatment planning, equipment performance, treatment delivery, etc., thereby improving dosimetric and geometric accuracy and the precision of dose delivery. This improves radiotherapy results (treatment outcomes), raising tumour control rates as well as reducing complication and recurrence rates [2]. Essentially, it can be divided into

- machine specific and
- patient specific QA

The **machine specific** part has to ensure optimal calibration of the LINAC's components, e. g. MLC leaves. There are checks which are performed daily, monthly or annually. So-called picket fence tests and consistency checks, such as a 4-field-box or a VMAT test plan, are applied, for example.

Originally, the 4-field-box is a conventional treatment technique that uses four static fields at gantry angles of 0° , 90° , 180° and 270° . It was often applied at tumours located in the lower pelvis¹¹ [21]. Figure 12 shows an example of the dose distribution for such a 4-field-box delivery. Nowadays, IMRT is more common in these cases, and is especially indicated for more complicated PTVs, e. g. in the head & neck region.

However, a 4-field-box (simple rectangular field is sufficient) as well as a VMAT with an irregular field are irradiated, for instance, onto a Delta⁴ phantom. By this means, it becomes possible to monitor the calibration of the LINAC in terms of dose and leaf positions, i. e. consistency, as well as the involved phantom over time.

In **patient specific QA**, the patient's treatment plan is irradiated onto a phantom on a regular basis in order to check the dose distribution (can be assisted by

¹¹ rectum, bladder, ovary, uterus, prostate

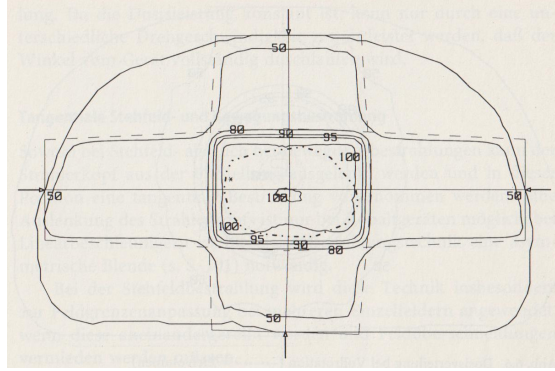


Figure 12: Example of dose distribution for a 4-field-box treatment [21].

independent dose calculation). One has to consider that not only too much absorbed dose represents a bad treatment delivery, but also too less dose. Over all fractions the patient receives, the total dose would not be accumulated. Thus the tumour would not be treated adequately.

Basically, the legal framework for QA in radiotherapy is given by the EC Council Directive 97/43 Euratom and its national interpretations. Amongst others, Klein et al. [22], Dieterich et al. [23] for robotic radiosurgery, Langen et al. [24] for tomotherapy, Kutcher et al. [25] as well as Podgorsak [2] provide additional guidelines and tolerance values.

1.6 Literature

Searching the literature, a number of studies on LINAC log files are found (see Tab. 1). However, only four deal with Elekta machines (Elekta AB, Stockholm, Sweden) as used at AKH Wien: Tyagi et al. [32], Pasler et al. [37], Kabat et al. [39] and Stanhope et al. [40]. That is, because log files were not available in the clinical mode of the Elekta LINAC until quite recently. In contrast, Varian Medical Systems Inc. (Palo Alto, U.S.) has been offering its so-called **DynaLog** log file system for some time. Besides, Tyagi et al. [32] programmed an application that interfaces to the Elekta machine in clinical mode via Elekta's **iCom Client interface D11** and an Ethernet connection. Pasler et al. [37] aimed for a machine specific QA, and therefore using the service mode was reasonable.

Already in 2002 Litzenberg et al. [26] presented a software which compares actual

Table 1: Literature on LINAC log files and key issues (studies using Elekta machines highlighted in bold).

Reference	Year	Log file analysis	Software development	QA implementation	Correlation analysis	Dose recalculation
Litzenberg et al. [26]	2002	yes	yes			
Agnew et al. [27]	2012			yes		
Agnew et al. [28]	2014	yes				
Kerns et al. [29]	2014	yes			yes	
Park et al. [30]	2014				yes	
Park et al. [31]	2015				yes	
Tyagi et al. [32]	2012		yes			yes
Calvo-Ortega et al. [33]	2014					yes
Qian et al. [34]	2010					yes
Sun et al. [35]	2012					yes
Defoor et al. [36]	2015					yes
Pasler et al. [37]	2015	yes	yes		yes	
Eckhause et al. [38]	2015	yes	yes			
Kabat et al. [39]	2016	yes				
Stanhope et al. [40]	2016					yes

MLC leaf positions for each leaf, recorded by means of DynaLog log files, to the expected positions resulting from treatment planning. Also fluence images were created from this field-information in order to establish a pretreatment fluence verification system. Dynamic MLC was the chosen modality. They concluded that their tools would allow for an automation of QA checks, resulting in a saving of time.

Agnew et al. [28] went one step further and investigated mean and standard deviation (SD) of the positional leaf error over time. They monitored the MLC daily performance (positioning accuracy) of two Varian LINACs over a one year period. The group reported average MLC positioning errors (± 1 SD) with a magnitude of 0.004 ± 0.003 mm (rotational picket fence (PF) test) and 0.004 ± 0.011 mm (static PF test), derived from the log file data. The errors obtained by the log files had a lower range (indicated by the SD) than the related electronic portal imaging device (EPID)-based ones which were: ± 0.025 mm (rotational), ± 0.039 mm (static). Furthermore, it was stated that the log files may not detect errors resulting from the t-nut or the drive motor (wear/tear) of the MLC, in contrary to EPID measurements. This may be due to the fact that the leaf positions were only calculated from the number of turns on the motor.

The impact of various mechanical and treatment parameters on the uncertainty in delivery has also been investigated. In the literature this is referred to as cor-

relation analysis. For example, mean and maximum leaf speed, gantry speed and mean leaf error already turned out as a factor (see the multi-institution evaluation by Kerns et al. [29]). According to Park et al. [30], [31] as well as Tyagi et al. [32], accelerations of leaves and gantry have a great impact on VMAT performance (Tyagi et al. [32] found a mean MLC error (± 1 SD) of 0.00 ± 0.59 mm from log file data). Also the influence of gravity due to an EPID, gantry or MLC carriage sag was studied. In an EPID-based work Rowshanfarzad et al. [41] reported a maximum sag in MLC leaf bank assemblies of around 1 mm.

Calvo-Ortega et al. [33], Qian et al. [34], Sun et al. [35] and Defoor et al. [36] are describing a log file based procedure for patient DVH¹² based IMRT QA. In other words, the log files are used to recalculate the actual patient dose distribution during every treatment with the TPS. Since there are no requirements for physical measurements with this method, all the calculations must be done based on the MLC leaf positions, collimator angle, gantry angle, and cumulative dose per control point that have been recorded in the MLC log file [36]. In particular, Defoor et al. [36] found the DVHs of the log files from two VMAT beams indistinguishable from those of the treatment plan. Consequently, the dose distribution was hardly affected. Besides, the MLC leaves showed a mean root mean square (RMS) deviation of 0.27 mm.

The two latest studies come from Pasler et al. [37] and Eckhause et al. [38]. Pasler et al. [37] present a multi-institutional study in which an artificial dynamic benchmark plan for VMAT is applied. The mean leaf error (± 1 SD), obtained by log file analysis, was 0.3 ± 0.2 mm for all Elekta LINACs investigated. They are concluding that log files serve as an important additional QA measure to understand and visualise dynamic LINAC parameters, namely dose rate, gantry speed and movements of collimator jaws and MLC leaves. Eckhause et al. [38] also conducted a multi-institutional survey on LINAC log files, however, for Varian units. This team targeted a patient as well as machine specific QA program. Evaluation of machine performance over time (IMRT plan) yielded a SD of 0.33 mm via the EPID measurement and < 0.12 mm via log files for all LINACs.

The most recent input on the topic of LINAC log file usage are two abstracts from the 58th annual meeting of the American Association Of Physicists In Medicine

¹² DVHs summarize the information contained in a three-dimensional treatment plan [5].

(AAPM) in 2016: Kabat et al. [39] and Stanhope et al. [40], both utilising Elekta LINACs. The former deals with LINAC consistency QA in IMRT. Besides a 2D gamma index calculated from fluence maps, an overall positional error for the MLC leaves was identified as 0.3 ± 0.08 mm (RMS). The group concluded that the use of Elekta log files for day-to-day evaluation of LINAC integrity and patient QA can be utilized to allow for reliable analysis of system accuracy and performance [39]. The latter is aiming for treatment planning and delivery QA. Stanhope et al. [40] specified to have used Elekta's **Log File Convertor R3.2**, recording dose rate, gantry angle and leaf position with VMAT plans. The plans were delivered onto an **ArcCHECK** phantom and afterwards the log files were reconstructed on its geometry. They stated, following certain reconstruction recommendations, the log-file technique is capable of detecting delivery errors with equivalent accuracy and less noise than the software **ArcCHECK QA** [40].

Of course, also non-standard treatment units such as CyberKnife and TomoTherapy device accumulate machine data, which is ready for an inspection.

Inoue et al. [42] studied residual patient movement, i.e. patient movement between image acquisitions, during intracranial image-guided robotic radiosurgery (CyberKnife). To be precise, the treatment log files recorded the timestamp, beam number and patient position expressed through three translational parameters and three rotational parameters in the acquired images. Information from the log files was used to calculate the time interval of acquired sequential images during the treatment and residual patient motion [42]. In addition, the resulting dosimetric effects were evaluated but considered to be minimal.

Handsfield et al. [43] are reporting on a phantom-less patient specific TomoTherapy QA via log files and a pre-treatment Monte Carlo-based secondary dose calculation. On the one hand, the planned dose is validated before the delivery, on the other hand, the delivered dose is analysed by means of an exit detector-based MLC sinogram and log file data. The log files contain ion chamber output, gantry and couch position as well as exit detector fluence. The MLC information is not recorded directly but identified by the exit detector. Then delivered parameters are compared to the parameters created by the TPS. The authors demonstrated that TomoTherapy treatments can be vulnerable to MLC deviations [43].

As referenced by Childress et al. [44], a similar problem as with Varian LINACs (see Agnew et al. [28] and above) was observed at a TomoTherapy site: The jaw sizes were varying during rotational delivery while the jaw position recorded on the log file recorded the same position as planned. It turned out that the jaw was driven by a stepping motor and its connection was loose, leaving the jaw freely moving, whereas stepping motor positions recorded on the log file remained unchanged. After that event, TomoTherapy uses servo motor for the jaws, which contains position feedback, to prevent this incident from happening again [44].

Log files have also been used in the proton world of radiotherapy, i. e. treatment with a proton (or carbon ion) beam. In 2013 Li et al. [45] reported on the use of treatment log files in spot scanning¹³ proton therapy as part of patient specific QA. The spot scanning proton beam delivery system is part of the synchrotron at the MD Anderson Cancer Center of the University of Texas. Proton beam energies ranging from 72.5 to 221.8 MeV are available there. For a test treatment plan as well as 14 real patient treatments, log files of the spot positions (analogon to MLC leaf positions at LINACs) and MU values were recorded. The latter were validated by measurements with two ion chambers under reference conditions. Displacements from the planned spot positions were also compared with results from radiographic films and a 2D ion chamber array. The patient treatment logs were used to calculate delivered doses. The maximum dose difference between calculated dose to the patient based on the plan and recorded data was within 2% [45]. The mean spot displacement (x/y -direction) was -0.03 mm/-0.01 mm with a maximum of 1.68 mm/2.27 mm and a SD of 0.26 mm/0.42 mm. The total MU accuracy was within 0.1% of the planned MU values [45]. In conclusion, the group found the treatment log file as precise enough to serve as a QA tool to monitor variation in spot position and MU value, as well as the delivered dose uncertainty from the treatment delivery system [45]. In a follow-up paper, Zhu et al. [46], the effort towards developing an efficient and effective patient specific QA program, which is enriched by treatment delivery log files, was again documented.

¹³ Currently, the most common method of delivering scanning beam proton therapy, in which a pencil beam (spot) is magnetically scanned laterally to the beam direction (x/y) to create a large treatment field without introducing scattering elements into the beam path [46].

The latest article on the topic comes from the Centre for Proton Therapy, Paul Scherrer Institute (PSI) in Switzerland. Scandurra et al. [47] present a comprehensive analysis of clinical treatments of 37 patients delivered at Gantry 2 (energy range 70-230 MeV). The precision and accuracy of the log file values have been previously validated during machine commissioning and are thoroughly checked during the routine QA program [47]. From the log file data, the group reconstructed the 3D dose distribution on the patient anatomy using a TPS-independent dose calculation system. Afterwards, a comparison with the nominal planned dose was done, resulting in a 3D dose difference distribution from which a number of quantities related to the volume's voxels were calculated: maximum, minimum and mean dose differences; the percentage of all voxels within $\pm 1\%$ of the nominal dose (pass rate). Also a mean spot position deviation was determined. The mean pass rate was 96.4%. The mean spot position deviation derived from the log files showed a strong correlation with the delivery quality in terms of the pass rate. Besides, a small bug in the TPS water-equivalent range calculation could be identified with the TPS-independent dose calculation and an increase of the pass rate was found after a significant update in the treatment workflow was made. According to the article, the future direction of performing log file analysis at PSI includes the possibility of performing in vivo plan verification at the first fraction, potentially removing the need for comprehensive pre-treatment verification, and the use of the log file 3D dose distribution together with the CT of the day to accumulate dose in a more complete adaptive therapy program [47].

1.7 Purpose and aim

Intensity-modulated radiation therapy (IMRT) is the state of the art treatment technique in external beam radiotherapy. Using the multi leaf collimator (MLC), a highly conformal delivery with steep dose gradients and a minimal dose to organs at risk (OAR) can be realised. Accuracy (and reproducibility) of certain parameters, such as gantry angle, collimator jaw and MLC leaf positions, dose rate or electron flux (from the electron gun)¹⁴ is of outmost importance to deliver sophisticated treatment plans adequately. Currently, quality assurance (QA) procedures rely

¹⁴ Does it decline during the service life of the gun?

mostly on external phantom-based measurements.

However, a phantom-based QA may have shortcomings. Handsfield et al. [43] are mentioning the inability to test for tissue heterogeneity dose calculation errors, the inability of the commonly used gamma metric to detect clinically relevant dose deviations, the limited generalizability of the 2D measurement to the 3D delivered dose and the fact that pretreatment measurements cannot account for delivery errors that occur during treatment. In addition, phantom-based QA requires a significant time commitment, requiring dedicated machine time for phantom setup and QA testing [43].

Be that as it may, electronic log files, which originate from the linear accelerator (LINAC) or MLC controller offer promising novel options for QA. Via this methodology, a variety of machine parameters can be recorded during the treatment, e.g. leaf positions. Utilising these log files might mean a reduction of phantom-based dose measurements in patient specific QA as they are currently performed on a regular basis.

Until a short time ago, Elekta LINACs were not capable of acquiring log files in the clinical mode (only possible in the service mode) of the machine. Data which is collected in the clinical mode, too, was officially only available through Elekta IntelliMax, a so-called intelligent device management (IDM) system. For example, every 15 seconds Elekta IntelliMax equipped LINACs automatically perform a system review and report findings securely to their designated Elekta service center [48]. However, this is a specific product by Elekta and the customer is only provided selected information. In addition, there was another software available, named `LINACWatch`, distributed by QualiFormeD SARL (La Roche Sur Yon, France). This software decrypts temporal tracking files and automatically analyzes them by comparing them in real time and in background (batch) processing to the planned treatment described in the `DICOM RTplan` associated with the planned beams [49].

Regarding log files from the service mode, readily available for every Elekta user, a computer program for processing was developed in-house. It converts the obtained `xml` files into plain text `csv` files, it visually displays leaf positions and on top of that compares the plan values contained in the machine-readable `dicom` files to the logged real values.

The major aim of this MSc thesis was to validate these electronic Elekta LINAC and MLC controller log files by means of several chosen test plan irradiations. The study duration was scheduled for six months. The anticipated conclusion was that log files, once clinically available for Elekta LINACs, might be a valid source of information which can be added to established QA procedures.

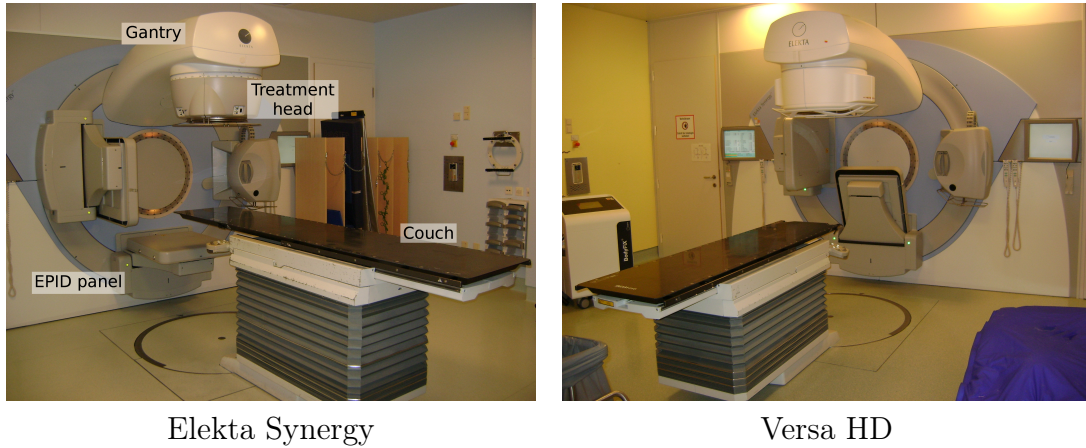


Figure 13: LINACs and treatment rooms.

Table 2: Technical overview of Elekta LINACs used.

LINAC	Model	Head	No. of leaf pairs	Leaf width	X-jaws
B	Versa HD	Agility	80	5 mm	no
D	Elekta Synergy	MLCi2	40	10 mm	yes

2 Materials and Methods

2.1 LINACs

Two digital LINACs, produced by Elekta AB (Stockholm, Sweden), were used in this study: one **Versa HD** and one **Elekta Synergy** model (see Fig. 13 and Tab. 2). In accordance to the naming convention used at the Department of Radiation Oncology, AKH/Medical University of Vienna, the two LINACs are also referred to in this text as **B** and **D**. LINAC B is capable of delivering photon energies of 6 as well as 10 MV in flattened (FF) and unflattened mode (FFF), i. e. 6FF (with flattening filter), 6FFF (flattening filter free), 10FF and 10FFF. LINAC D has 6, 10 and 18 MV, all FF only. They were equipped with different treatment heads: Agility (Versa HD) and MLCi2 (Synergy).

Since the former pairing is the more recent one (Agility is Elekta’s follow-up model of the MLCi2), operating more accurately, additional specifications are given below.

2.1.1 Versa HD (Agility) - additional specifications

The distance from source to isocentre is 100 cm. In contrast to the Synergy model, Versa HD provides a higher dose rate ($\hat{=}$ MU/min at isocentre, depending on energy). Its Agility treatment head offers a maximum field of view (FOV) of 40×40 cm². The leaves (80 pairs, 5 mm in width) can reach a speed of up to 6.5 cm/s¹⁵ with a leaf position accuracy of 1 mm at isocentre (conversely, another manual [50] quotes ± 0.3 mm), 0.5 mm root mean square (RMS). The leaf position repeatability is lower than 0.5 mm [51]. The treatment head does not contain jaws in *X*-direction. Of course, *Y*-jaws are utilised as the MLC leaves would only allow a discrete adjustment of the field size in *Y*-direction. This sculpted collimators, orthogonal to the direction of leaf motion, can move at up to 9 cm/s [37]. The main reason for the higher accuracy lies in the so-called Rubicon leaf positioning system: Ultraviolet light is sent to a ruby attached to the leaf. Infrared light is emitted and can be detected via a camera, filtering out the other ranges of the spectrum. By comparison, MLCi2 uses a halogen lamp and a simple reflection of visible light.

2.1.2 Operation

The test plans (which will be described in Sec. 2.4, 2.5, 2.6 and 2.7) were loaded into the LINAC's control system from the record and verify system *Mosaiq* (Elekta AB, Stockholm, Sweden). Irradiations were performed in the service mode of the machine ("copy to service mode") since an acquisition of log files was not possible in the clinical mode.

2.2 Delta⁴ phantom and gamma index

The ScandiDos Delta⁴ phantom (ScandiDos AB, Uppsala, Sweden) is a cylindrical phantom ($\varnothing 220 \times 400$ mm²) made of polymethylmethacrylate (PMMA)¹⁶, containing two perpendicularly arranged (cross-shaped) diode arrays/electrometers for radiation detection (see Fig. 14). To be precise, one of the arrays is called the main unit, the other one consists of two so-called wing units. They are all

¹⁵ sum of leaf movement and dynamic leaf guide movement speed

¹⁶ Its density of 1.19 g/cm³ is very similar to the human body's cancellous bone.

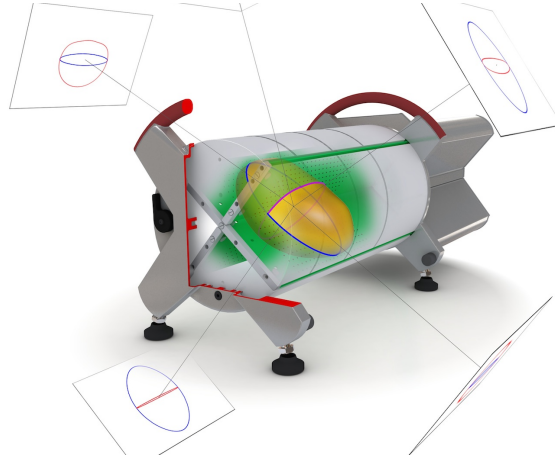


Figure 14: ScandiDos Delta⁴ phantom, schematic [53].

removable from the phantom, which is necessary for the calibration process. The 1,069 detectors, in total, are p-type Si. They are arranged on a $200 \times 200 \text{ mm}^2$ grid per array. In the outer regions the pitch is 10 mm, 5 mm in the inner regions. The resolution is 0.01 mGy with a dose range from 1 mGy to unlimited [52].

Via a trolley, the phantom was positioned at the front end of the treatment couch (no extensions attached) and then aligned with the isocentre by means of the laser projectors (see Fig. 15) as well as the adjustable feet of the phantom. The accompanying software **ScandiDos Delta4** was operated on a notebook plugged to the phantom via an Ethernet cable. In addition, a coaxial cable providing a trigger signal connected LINAC and phantom.

The reference data is obtained from the treatment planning system (TPS)-based dose calculation of the particular plan (.dcm, RTDOSE).

The measured data is assessed by the software following the concept of the so-called γ index, introduced by Low et al. [54]: For every measurement point on the detector plates, two quantities are assessed: the **dose deviation** DD (%) from the plan value and the so-called **distance to agreement** DTA (mm) (how far away is the point that has actually received the planned dose?). The latter is especially important in regions with steep dose gradients, where also small spatial errors result in a significant difference between plan and delivery. Next the two are mathematically combined to the **gamma index** γ . It acts as a pass/fail criterion, which also has a geometrical representation by the surface of an ellipsoid. Figure 16

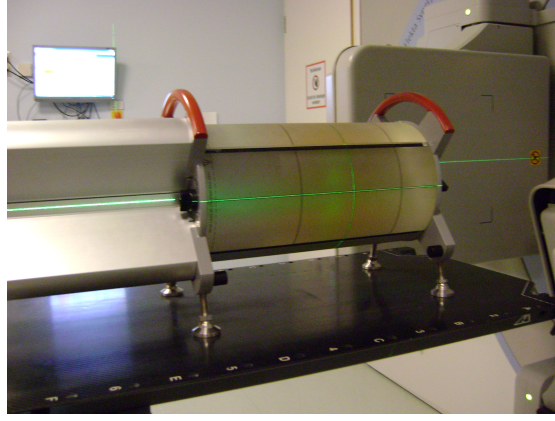


Figure 15: Delta⁴ phantom on treatment couch, aligned by means of laser projectors.

and the formulas below illustrate the principle.

$$\gamma(r_m^{\rightarrow}) = \min \{ \Gamma(r_m^{\rightarrow}, r_c^{\rightarrow}) \} \forall \{ r_c^{\rightarrow} \} \quad (19)$$

where

$$\Gamma(r_m^{\rightarrow}, r_c^{\rightarrow}) = \sqrt{\frac{r^2(r_m^{\rightarrow}, r_c^{\rightarrow})}{\Delta d_M^2} + \frac{\delta^2(r_m^{\rightarrow}, r_c^{\rightarrow})}{\Delta D_M^2}} \quad (20)$$

$$r(r_m^{\rightarrow}, r_c^{\rightarrow}) = |r_c^{\rightarrow} - r_m^{\rightarrow}| \quad (21)$$

and

$$\delta(r_m^{\rightarrow}, r_c^{\rightarrow}) = D_c(r_c^{\rightarrow}) - D_m(r_m^{\rightarrow}) \quad (22)$$

is the difference between dose values of the calculated (D_c) and measured (D_m) distributions, respectively [54]. r_m^{\rightarrow} denotes a measurement point, r_c^{\rightarrow} a point calculated in treatment planning. ΔD_M stands for the dose-difference criterion and Δd_M for the *DTA* criterion. Usually, they are chosen as $\Delta D_M = 3\%$ and $\Delta d_M = 3$ mm. It holds that

$$\gamma(r_m^{\rightarrow}) \leq 1, \quad \text{dose distribution passes} \quad (23)$$

$$\gamma(r_m^{\rightarrow}) > 1, \quad \text{dose distribution fails} \quad (24)$$

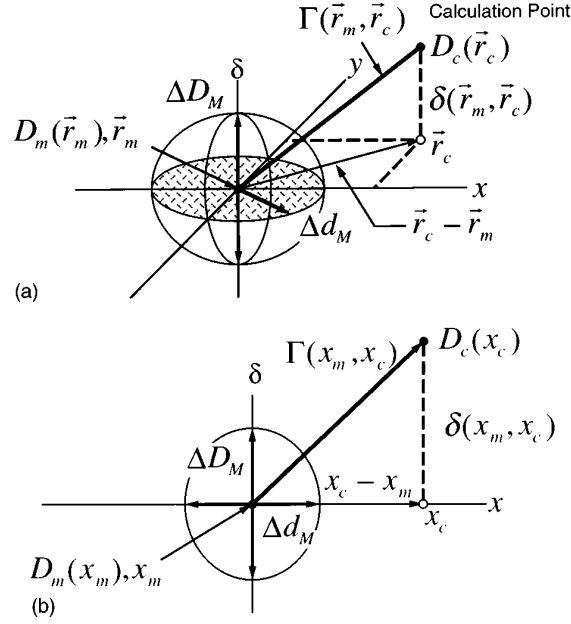


Figure 16: Geometric representation of gamma index γ : (a) two-dimensional representation, (b) one-dimensional representation [54].

this combined ellipsoidal dose-difference and distance-to-agreement test.

Finally, the **gamma passing rate** GPR is the percentage of measurement points which showed a $\gamma \leq 1$. A common limit is 90%.

2.3 Log files and in-house software

LINAC and MLC controller log files were acquired during every irradiation in this study. This could only be realised in the service mode of the machine where this is called service graphing. The mechanical and electrical parameters that were chosen to be recorded, e.g. MLC leaf positions, electron gun current, are listed in Tab. 3 with a short description. The particular items and parts had to be entered. After the acquisitions, the `xml` type log files were saved at a remote computer via LAN.

As for the processing of the log files, an in-house software named **LogAnalyzer** was developed by Andreas Moser. Figure 17 shows a screenshot. First, the treatment technique (volumetric-modulated arc therapy (VMAT), IMRT or conventional) and the leaf width (5 or 10 mm) has to be picked. Next the plan file (`.dcm`,

Table 3: Configuring service graphing in LINAC’s service mode: items and parts for logging (item 2100 only on Elekta Synergy LINAC D).

Item	Part	Name	Description
70	4	gantry	gantry angle
all leaves	129		leaf position
80	4	jaw	jaw position
85	4	jaw	
44	4	dose rate 1	
45	4	dose rate 2	
33	4	beam mu 1	<u>monitor</u> <u>units</u>
34	4	beam mu 2	
217	4	gun i mon	electric gun current
2200	111	prf pause	<u>pulse</u> <u>repetition</u> <u>frequency</u>
2100	227	actual MLC tolerance	
164	4	2RI control	homogeneity of beam
165	4	2T	

RTPLAN) as well as the corresponding log files (.xml) have to be loaded for each field. A VMAT plan offers two possibilities in terms of evaluating the deviations of the leaf positions from the test plan: nearest neighbour or linear interpolation.¹⁷ The former was chosen in this study. From the recorded leaf positions (all leaves, 129) as well as from the electric gun current (217, 4), the applied version of LogAnalyzer was capable of editing/calculating the following quantities:

- mean leaf error
- maximum leaf error
- leaf error standard deviation
- leaf RMS
- gun current

To be precise, the gun current is obtained as a list of chronological values (mA) throughout the irradiation process for each field, i. e. discrete measuring points

¹⁷ The frequency in which the data is logged in the files (4 Hz, $T = 250$ ms) differs from the frequency of positioning commands in the plan files.

according to the frequency of logging. The mean leaf error and its derived quantities (maximum, standard deviation and RMS) are shown as a diagram and table depicting the behaviour of every leaf per bank ($X1$ and $X2$) and field (see Fig. 17). The underlying equations are supposed to be:

$$d_{mean} = \frac{1}{n} \cdot \sum_{i=1}^n d_i \quad (25)$$

$$d_{max} = d_i | \text{highest absolute value} \quad (26)$$

$$d_{sd} = \sqrt{\frac{1}{n-1} \cdot \sum_{i=1}^n (d_i - d_{mean})^2} \quad (27)$$

$$d_{rms} = \sqrt{\frac{1}{n} \cdot \sum_{i=1}^n d_i^2} \quad (28)$$

with d_i denoting the deviation of one single discretely logged leaf position i ($i = 1 \dots n$) from the plan.

2.4 Static picket fence test

In a picket fence (PF) test, a rectangular slit formed by the MLC leaves is either moved discretely for a number of times (static test) or moved continuously (dynamic test, see Sec. 2.6.1) during irradiation so that a picket fence pattern is obtained.

A static PF test was designed with the **Oncentra** TPS (Elekta AB, Stockholm, Sweden) under the assumption of a cubic water phantom aligned with the isocentre (D100). Five rectangular fields were planned. The specifications are shown in Tab. 4. As depicted, the slit ($x2 - x1$) was chosen 2 cm wide. The photon beam energy was set 6 MV.

The gantry was positioned at 0° , the couch (without any extensions attached) was moved out of the field as well as lifted to the height of the isocentre. The test was irradiated onto the integrated electronic portal imaging device (EPID) on a weekly basis (as done in machine specific QA), attended by log file recording. The EPID software **iviewGT** (Elekta AB, Stockholm, Sweden) acquired images (“single

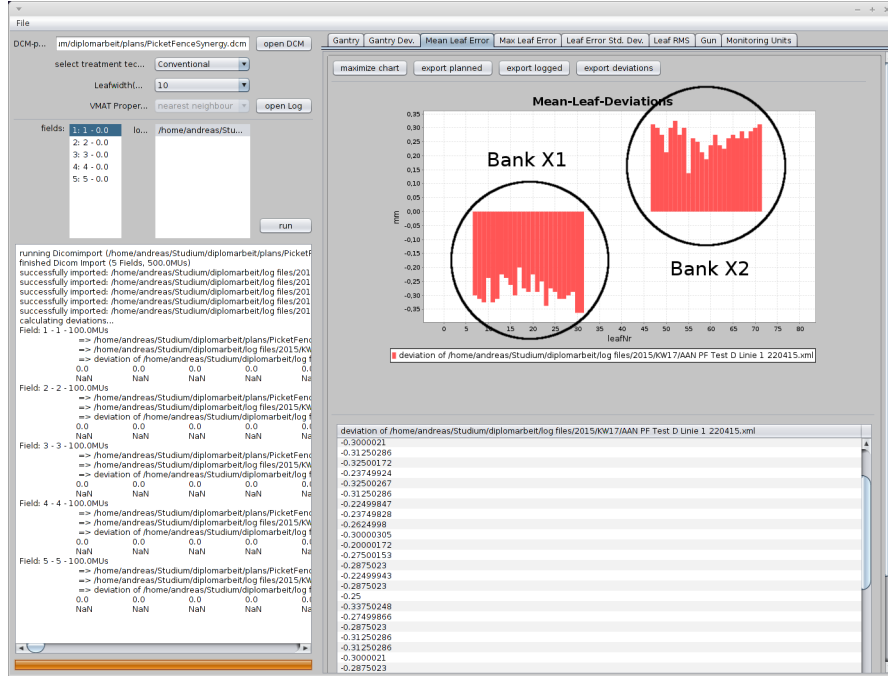


Figure 17: Screenshot of LogAnalyzer by Andreas Moser, with annotations: Evaluation of a static picket fence (PF) test at LINAC D, tab of mean leaf error for field 1 shown.

Table 4: Specifications of the static picket fence (PF) test: MLC leaf positions x (cm) and collimator jaw positions X, Y (cm).

Field	$x1$	$x2$	$X1$	$X2$	$Y1$	$Y2$
1	-12	-10	-12.5	-9.5	-12.5	12.5
2	-3	-1	-3.5	-0.5	-12.5	12.5
3	-1	1	-1.5	1.5	-12.5	12.5
4	1	3	0.5	3.5	-12.5	12.5
5	10	12	9.5	12.5	-12.5	12.5

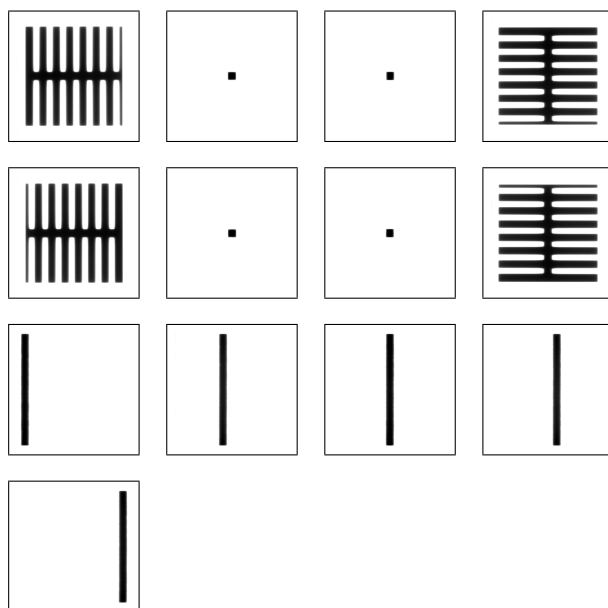


Figure 18: Static PF test sequence: 13 single captures by the EPID software `iviewGT`; combs, squares and PF pattern.

capture”), which then were exported into the `tiff` format and saved at a remote computer via LAN.

The evaluation was performed using `MLC Soft EPID` by PTW Freiburg GmbH (Freiburg, Germany). Besides the five rectangular fields producing the picket fence pattern, the software needs a few other single exposures of combs and squares on the EPID in order to establish a reference coordinate system, resulting in a total of 13 images. This sequence is presented in Fig. 18. After that, the program is able to calculate leaf positions¹⁸ and their deviations from the plan (compare mean leaf error, Sec. 2.3). In a graphical representation, errors ranging from 0.5 to 1 mm are highlighted yellow, those larger than 1 mm are red.

2.5 Consistency checks

Two different consistency checks were also applied on a weekly basis (plus recording of log files): a 4-field box with a $20 \times 28 \text{ cm}^2$ rectangular field, irradiated from 0° , 90° , 180° and 270° and a head & neck VMAT plan with an irregular field, created

¹⁸ peaks and FWHM of blackening pattern are analysed

Table 5: Acceptance criteria for consistency checks following the concept of γ index.

	<i>DD</i>	<i>DTA</i>	<i>GPR</i>
LINAC B	2%	2 mm	>90%
LINAC D	3%	3 mm	>90%

Table 6: Specifications of the dynamic PF test: MLC leaf positions x (cm) and collimator jaw positions X, Y (cm).

CP	$x1$	$x2$	$X1$	$X2$	$Y1$	$Y2$
1	-12.5	-11.5	-20.0	20.0	-12.5	12.5
2	11.5	12.5	-20.0	20.0	-12.5	12.5

for a former patient, performed as a full arc (180° to 180°) rotation by the gantry.

The Delta⁴ phantom was utilised for experimental verification. Table 5 shows the acceptance criteria for LINACs B and D, previously described in Sec. 2.2, which represented the basis for the evaluation of the consistency checks. The limits were chosen tighter for LINAC B (2%/2 mm) than LINAC D (3%/3 mm), because it operated more accurately with the Agility treatment head.

2.6 Additional tests

Two additional tests were performed. These irradiations took place at least three times to evaluate the influence of daily variations. Again, log files were also recorded.

2.6.1 Dynamic PF test

A dynamic PF test was already available. It had been created in Monaco¹⁹ (Elekta AB, Stockholm, Sweden). Table 6 shows the specifications of this test plan, containing two control points (CPs). In contrast to the static PF test, the slit (formed by the MLC leaves) sweeps from the first to the second CP with the irradiation being in progress. The slit width was 1 cm. Irradiated onto the EPID, such an acquisition is anticipated to display horizontally aligned rectangles, when seen

¹⁹ a TPS based on Monte Carlo algorithms

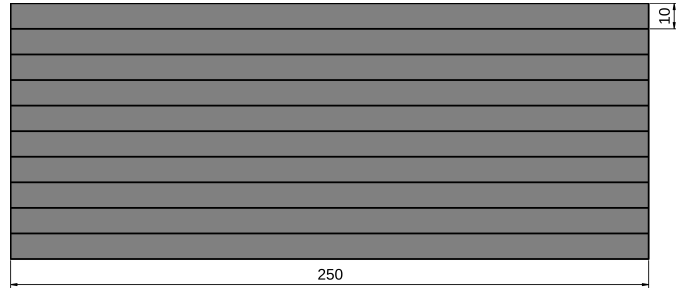


Figure 19: Anticipated result for dynamic PF test at LINAC D: 10 rectangles (leaf pairings) are shown, dimensions in mm.

through beam's eye view (BEV), which represent the gap between two opposing leaves. The length of a rectangle (in original scale) is given by $x2$ of CP 2 minus $x1$ of CP 1, the width is given by the leaf width. Darker lines (more blackened) in between them result from leakage radiation through the space between neighbouring leaves (although leakage radiation is tried to be minimised by the MLC design). In other words, a picket fence pattern rotated by 90° can be identified (see Fig. 19).

The images of the dynamic test were analysed with the public domain image processing program *ImageJ*. To be precise, using the plugin "Specify ROI" (Edit>Selection>Specify), a rectangular area was defined to read out the mean gray value²⁰ of the pixels for every leaf pairing. This was done manually. However, it should be possible to automatise this analysis by means of a script.

2.6.2 Analysis of the influence of gravity

In order to evaluate the influence of gravity on the positioning accuracy of the MLC leaves, the static PF test (as described in Sec. 2.4) was also performed at gantry angles of -90° and $+90^\circ$.

2.7 Sensitivity analysis

The sensitivity of the three measurement methods (log files, EPID, Delta⁴ phantom) was investigated by means of implementing leaf positioning errors in the

²⁰ Note that the program defines mean gray value in such a way that the values are higher for less blackening.

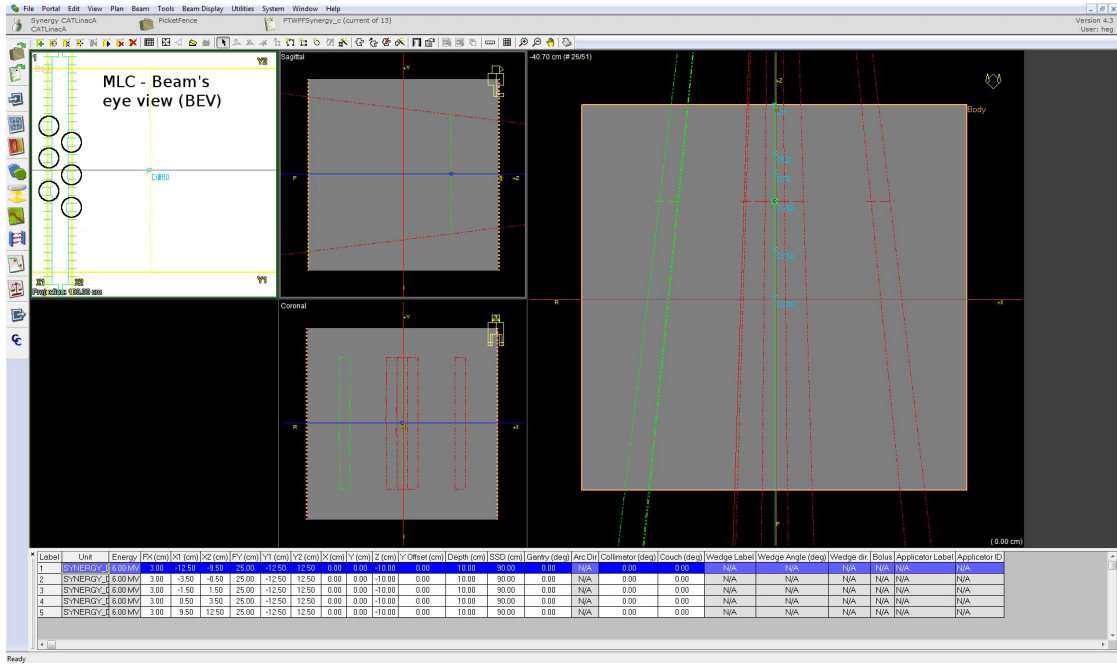


Figure 20: Screenshot of treatment planning system **Oncentra**, with annotations: Implementing leaf positioning errors in the static PF test plan for LINAC D (sensitivity test plan **c**, field 1 chosen).

static and dynamic PF test plans, previously described in Sec. 2.4 and Sec. 2.6.1, respectively.

For the five rectangular fields of the static test, this could be realised using the **Oncentra** TPS where it was possible to manipulate single leaves (see Fig. 20). Three different sensitivity test plans were introduced:

- test plan **a**
- test plan **b**
- test plan **c**

In test plan **a**, all leaves of the left MLC bank forming the left side of the slit were shifted to the left side in three steps: $x1 - 0.5$ mm (named **a1**), $x1 - 1$ mm (**a2**) and $x1 - 2$ mm (**a3**). In plan **b** (**b1**, **b2**, **b3**), only every third leaf was treated this way. To be precise, the shifted leaf no. (through BEV, from top to bottom) were: 18, 21, 24, ... 63 for LINAC B, bank X1 and 10, 13, 16, 19, 22, 25, 28 and 31

Table 7: Specifications of sensitivity test plan **c**: MLC leaf no. (through BEV) for introduced negative errors.

	LINAC B		LINAC D	
	X1	X2	X1	X2
-0.5 mm	15	17	35	37
-1.0 mm	19	21	39	41
-2.0 mm	23	25	43	45

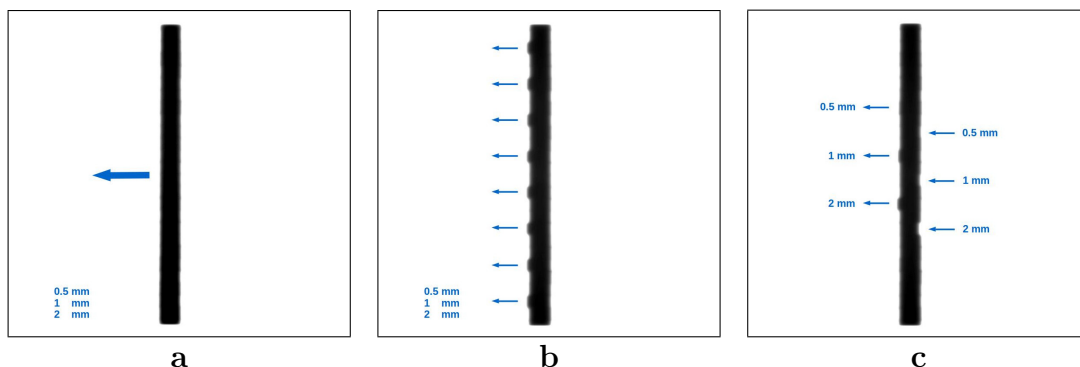


Figure 21: Test plans for sensitivity checks: **a** (whole left bank moved), **b** (every third leaf moved) and **c** (both banks involved).

for LINAC D, bank X1. Plan **c** involved both banks and negative errors of 0.5, 1 and 2 mm contained in one irradiation (see Tab. 7 for the detailed specifications). Figure 21 illustrates the three test plans via an EPID image for one of the five fields.

Test plan **c** was mainly irradiated onto the EPID as this measurement method is capable of discriminating MLC banks and displaying single leaves. For the Delta⁴ phantom, working quite differently, a systematic error concerning one bank and a considerable number of leaves, i. e. plans **a** and **b**, was analysed.

As **Oncentra** was not capable of handling dynamic MLC features, and as it was also not possible to manipulate single leaves in **Monaco**, the software **DCMTree** was used to create an erroneous dynamic PF test plan **c**. The slits, formed in CP 1 and 2, were altered in the aforementioned way. Besides the MLC leaf positions, this program enables editing of various parameters stored in the **dicom** file.

In the same way as the additional tests, each sensitivity test plan was irradiated at least three times to evaluate the influence of daily variations.

2.8 Data analysis - leaf error definitions

Analysing the data output of LogAnalyzer as well as MLC Soft EPID, a number of quantities (leaf errors) were calculated. Definitions are as followed:

- **mean measurement leaf error**

average of mean leaf errors (as described in Sec. 2.3 and Eq. 25) over all irradiated fields of static PF test and 4-field-box, respectively (equals mean leaf error for VMAT);

alternatively, the absolute values of the mean leaf errors can be averaged:

- **mean measurement leaf error (absolute)**

- **mean measurement bank error**

average of mean measurement leaf errors over all leaves of one bank

- **mean leaf positioning error**

result of averaging mean measurement bank errors over all measurements

The mean measurement bank error and its development in time was assessed. Furthermore, linear correlations between log file and EPID data were investigated utilising the Pearson correlation coefficient r (for a sample). In general, r is given by [55]

$$r = \frac{1}{n} \cdot \sum_{i=1}^n \frac{x_i - \bar{x}}{s_x} \cdot \frac{y_i - \bar{y}}{s_y} \quad (29)$$

with x_i and y_i denoting a pair of simultaneously measured values of a series which are to be contrasted (\bar{x} , \bar{y} ... mean, s ... standard deviation). It holds that

$$-1 \leq r \leq 1 \quad (30)$$

1 means a total positive correlation, -1 a total negative, and 0 means no correlation.

The mean leaf positioning error acts as an overall measure of positioning accuracy.

Out of ScandiDos Delta4, the gamma passing rate GPR was used as comparative data to the log file based mean measurement bank error and its standard deviation

(4-field-box and VMAT).

Statistical significance (e. g. in the sensitivity analysis) was assessed applying the standard deviation (SD): Significance was assumed for a value greater than or equal 2 SDs above the “noise” (e. g. mean measurement bank error).

In order to evaluate the electron gun current, a linear regression model working with the method of least squares was used. Its results are two regression coefficients, α and β , which represent the line’s intercept and slope (compare linear equation $Y = \alpha + \beta x$). Two more quantities were calculated:

- coefficient of determination R^2
For a bivariate regression it equals r^2 and ranges from 0 to 1. It can be understood as a measure of the model’s power.
- standard errors of the regression coefficients, σ_α and σ_β ,
which make it possible to estimate the significance of the coefficients via a so-called t-test using the formula [55]

$$\frac{|\hat{\beta}|}{\hat{\sigma}_{\hat{\beta}}} > t_{1-\alpha/2}^{n-2} \quad (31)$$

The hat denotes the estimated value, and $\hat{\beta}$ can be replaced with $\hat{\alpha}$, resulting in the corresponding formula for the intercept. t is the quantile of the t-distribution for a sample size n and a level of significance α .

Table 8: Mean leaf positioning error and SD (both mm) for study duration.

Static PF test								
Log files					EPID			
	LINAC B		LINAC D		LINAC B		LINAC D	
	<i>X1</i>	<i>X2</i>	<i>X1</i>	<i>X2</i>	<i>X1</i>	<i>X2</i>	<i>X1</i>	<i>X2</i>
Mean	0.010	-0.002	-0.301	0.309	0.211	0.381	-0.355	-0.073
SD	0.014	0.010	0.036	0.033	0.095	0.055	0.125	0.143
4-field-box								
Log files								
	LINAC B		LINAC D					
	<i>X1</i>	<i>X2</i>	<i>X1</i>	<i>X2</i>				
Mean	0.002	-0.042	-0.296	0.291				
SD	0.029	0.036	0.045	0.041				
Head & neck VMAT								
Log files								
	LINAC B		LINAC D					
	<i>X1</i>	<i>X2</i>	<i>X1</i>	<i>X2</i>				
Mean	-0.159	-0.207	-0.022	-0.027				
SD	0.121	0.139	0.079	0.082				

3 Results

3.1 Static PF test, consistency checks

3.1.1 Mean leaf positioning error

Table 8 presents the log file based results for the mean leaf positioning error and its SD (average of mean measurement bank errors' SDs), obtained from the static PF test (including EPID data), the 4-field-box as well as the head & neck VMAT test plan. The MLC banks are denoted by *X1* and *X2*, respectively.

As depicted, LINAC B log files showed a lower error (0.010 mm *X1*/ -0.002 mm *X2*, 0.002 mm *X1*/ -0.042 mm *X2*) than LINAC D (-0.301 mm *X1*/ 0.309 mm *X2*, -0.296 mm *X1*/ 0.291 mm *X2*) for the tests containing static fields (static PF test, 4-field box). Quite the opposite was discovered for the VMAT: LINAC B yielded errors of -0.159 mm *X1*/ -0.207 mm *X2*, LINAC D -0.022 mm *X1*/ -0.027 mm *X2*.

Also for the static plans, the errors of LINAC D were located symmetrically

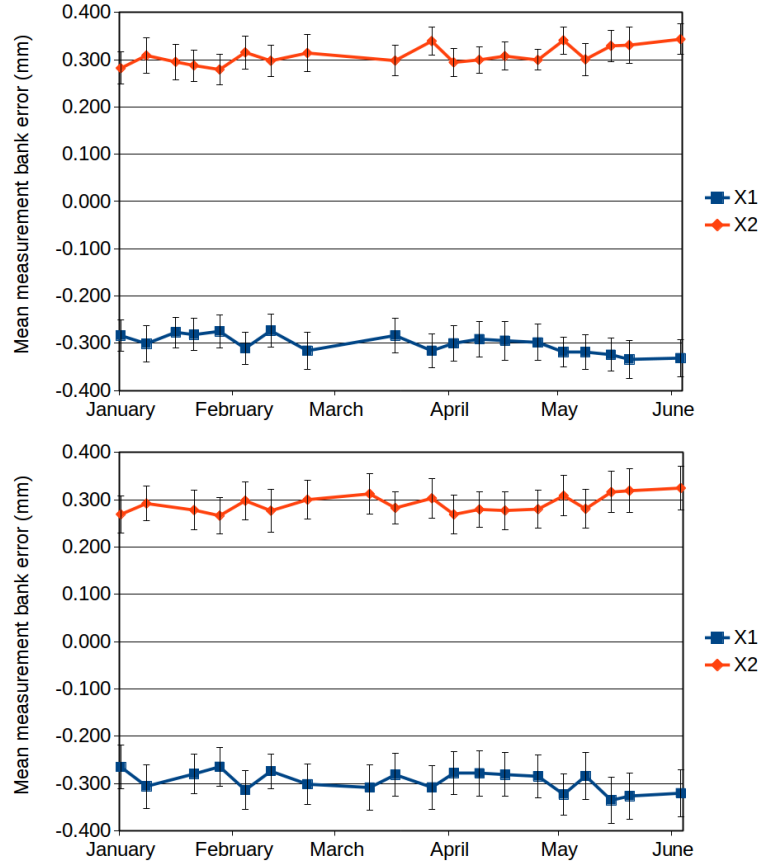


Figure 22: Mean measurement bank error (mm) ± 1 SD vs. time for static PF test (top) and 4-field-box (bottom) at LINAC D, calculated from log file data.

around 0 (see also mean leaf error in Fig. 17 and mean measurement bank error in Fig. 22). In other words, the leaves of bank *X1* as well as the leaves of bank *X2* were undershooting, with *X1* having a negative error and *X2* having a positive error. Hence the rectangular field actually irradiated onto the EPID was wider by about 0.6 mm.

Regarding the EPID data, rather different values for the mean leaf positioning error (static PF test) were obtained in comparison to the log files (LINAC B: 0.211 mm *X1*/ 0.381 mm *X2*, LINAC D: -0.355 mm *X1*/ -0.073 mm *X2*; Tab. 8).

3.1.2 Mean measurement bank error

Surprisingly, also the time development of the mean measurement bank error, calculated from the log files, did not agree with the observed EPID behaviour. Figures 23 and 24 illustrate the situation. The error bars represent 1 SD over the particular MLC bank (and are much larger for the EPID). The overall Pearson correlation coefficient r between the two series was around 0.27 (mean of 0.16, 0.31, 0.58 and $|-0.01|$); see Tab. 9 for the detailed relations between the MLC banks. Even smaller values were obtained between log files and Delta⁴ measurements (*GPR*) for the VMAT: around 0.06 (mean of $|-0.08|$, $|-0.03|$, $|-0.07|$ and 0.05), see Tab. 11. The 4-field-box ranged around 0.31 (mean of 0.17, 0.18, 0.41 and $|-0.46|$), see Tab. 10. Related scatter plots are presented in Fig. 25, 26 and 27. Besides, the Tab. 9, 10 and 11²¹ also reveal that the correlations between the banks $X1$ and $X2$ (log file data) were rather high with about 0.5 (mean of 0.53, 0.45 and 0.66) for LINAC B and even 0.9 (mean of $|-0.85|$, $|-0.95|$ and 0.88) for LINAC D.

Figure 28 opposes the SD of the mean measurement bank errors obtained for the VMAT irradiations at LINAC B to the corresponding development of the *GPR*. The second data point of bank $X2$ is an outlier caused by a single mean leaf error (= mean measurement leaf error) of higher value distorting the line of linear regression. Figure 29 shows the same results for the 4-field-box. Moreover, a similar behaviour applies for LINAC D.

3.1.3 Mean leaf positioning error (absolute)

Alternatively to the concept applied for Tab. 8, Tab. 12 displays the results for the mean leaf positioning error with absolute values of the mean leaf errors averaged over the fields of static PF test and 4-field-box, respectively. The SD is again given by averaging the banks' SDs over all measurements. Exactly the same absolute values were found for the log file data from LINAC D. In contrast, some absolute values for LINAC B were differing substantially. $X2$ - static PF test (0.010 mm) as well as $X1$ and $X2$ - 4-field-box (0.115 and 0.119 mm) were in a higher range;

²¹ Elements in these matrices that represent correlations of data sets with themselves ($r = 1$) as well as sets which are only compared in the reverse order are left blank.

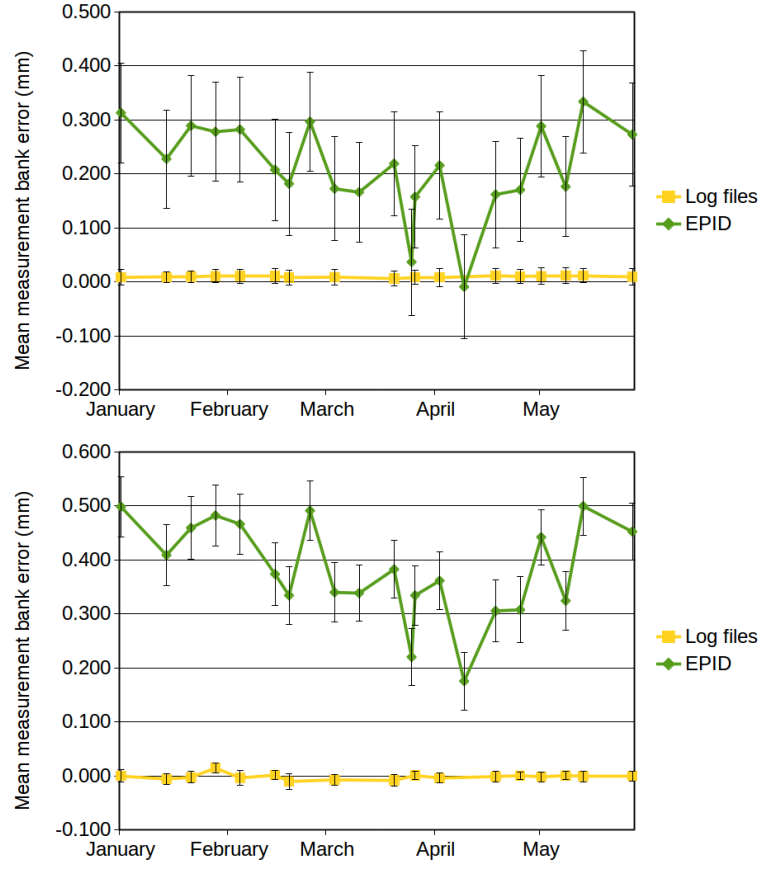


Figure 23: Mean measurement bank error (mm) ± 1 SD vs. time for static PF test at LINAC B: bank X1 (top) and X2 (bottom).

Table 9: Pearson correlation coefficients r for static PF test.

			Log files B		EPID B		Log files D		EPID D		
			X1	X2	X1	X2	X1	X2	X1	X2	
Log files	B	X1	0.53		0.16						
		X2			0.31						
EPID	B	X1			0.98						
		X2									
Log files	D	X1					-0.85		0.58		
		X2							-0.01		
EPID	D	X1							0.87		
		X2									

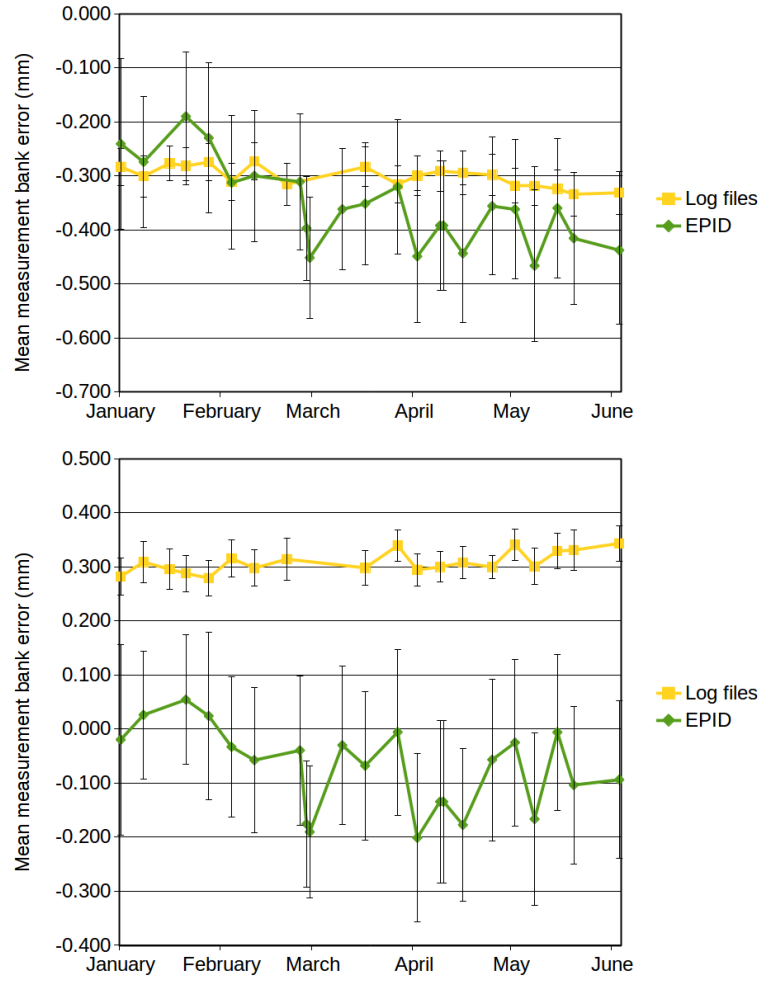


Figure 24: Mean measurement bank error (mm) ± 1 SD vs. time for static PF test at LINAC D: bank X1 (top) and X2 (bottom).

Table 10: Pearson correlation coefficients r for 4-field-box.

			Log files		Delta ⁴	Log files		Delta ⁴
			B		B	D		D
			X1	X2		X1	X2	
Log files	B	X1	0.45		0.17			
		X2						
Log files	D	X1			0.18	-0.95		
		X2						
						-0.46		

Table 11: Pearson correlation coefficients r for head & neck VMAT.

			Log files		Delta ⁴	Log files		Delta ⁴
			B		B	D		D
			X1	X2		X1	X2	
Log files	B	X1		0.66	-0.08			
		X2			-0.03			
Log files	D	X1				0.88		-0.07
		X2						0.05

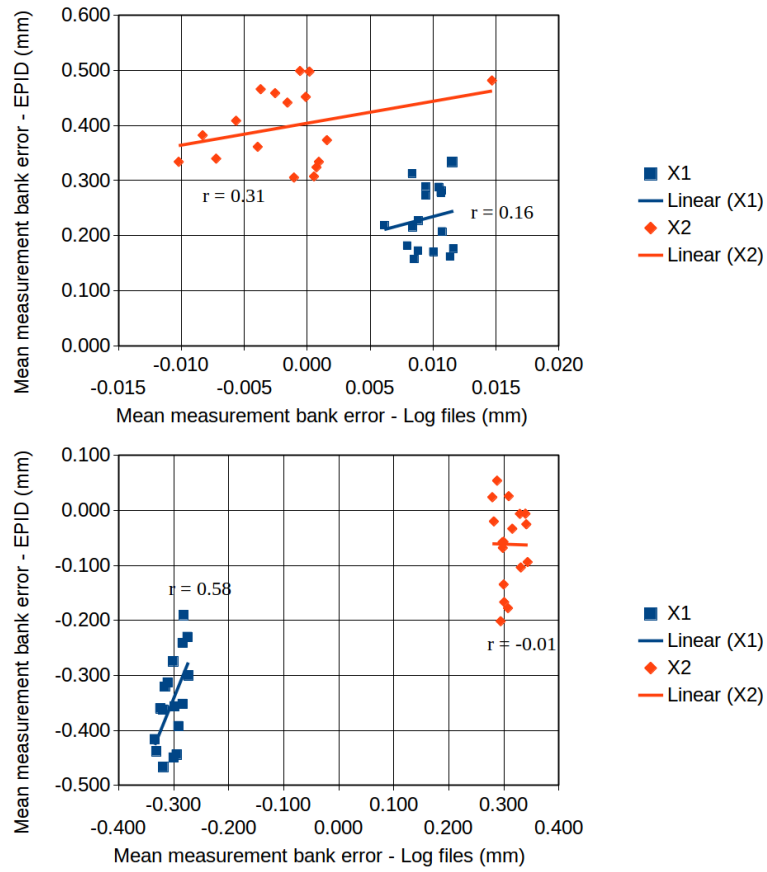


Figure 25: Mean measurement bank error (mm) for static PF test: scatter plot of log files and EPID, LINAC B (top) and LINAC D (bottom).

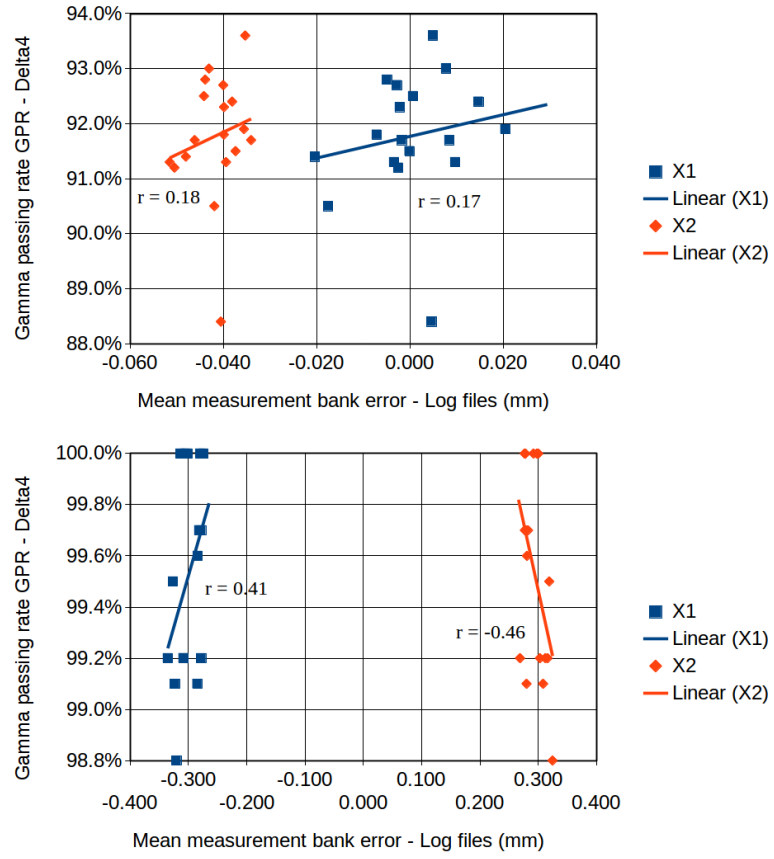


Figure 26: Mean measurement bank error (mm)/ *GPR* for 4-field-box: scatter plot of log files and Delta⁴ phantom, LINAC B (top) and LINAC D (bottom).

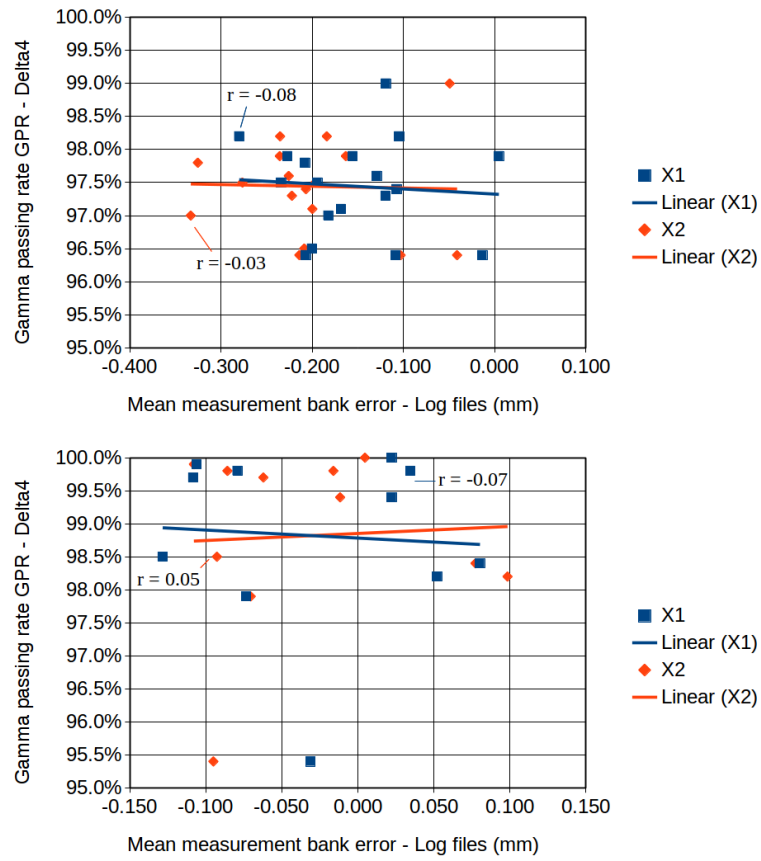


Figure 27: Mean measurement bank error (mm)/ *GPR* for head & neck VMAT: scatter plot of log files and Delta⁴ phantom, LINAC B (top) and LINAC D (bottom).

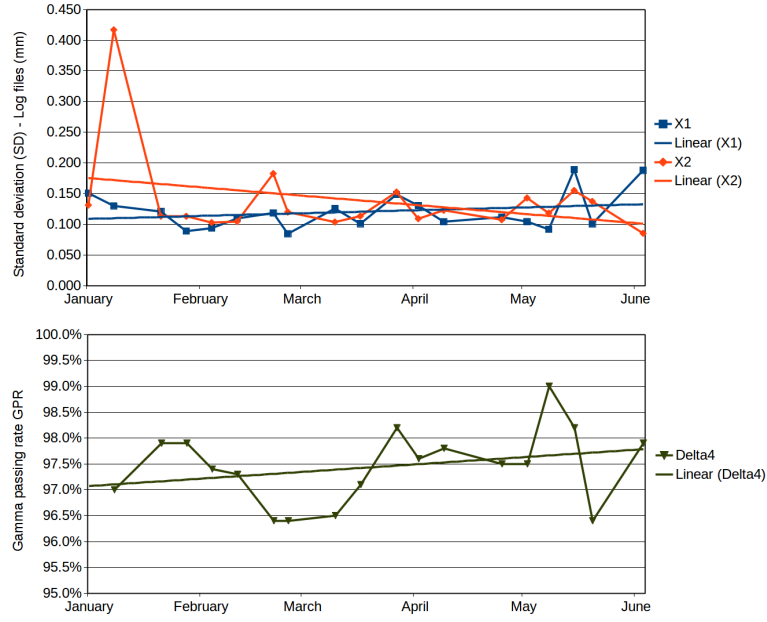


Figure 28: Standard deviation (SD) of mean measurement bank errors and gamma passing rate GPR vs. time for VMAT at LINAC B.

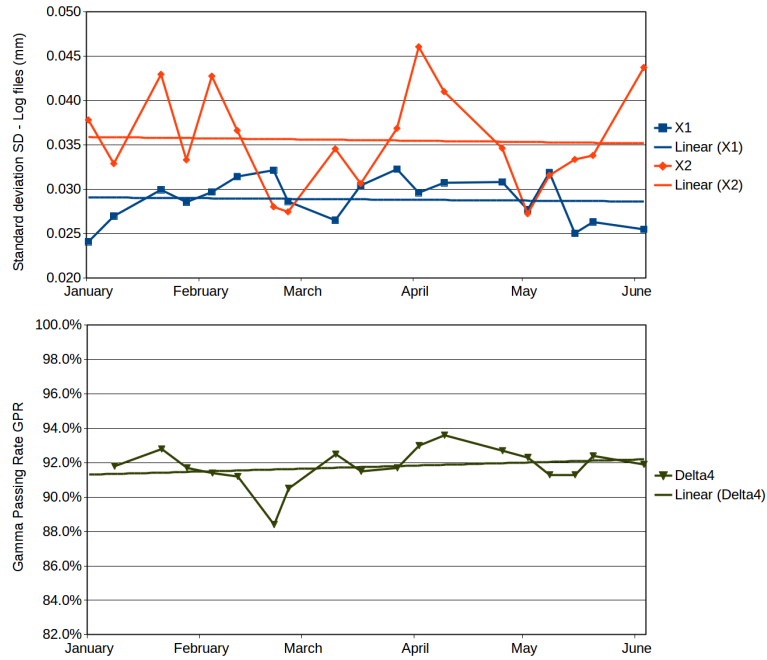


Figure 29: Standard deviation (SD) of mean measurement bank errors and gamma passing rate GPR vs. time for 4-field-box at LINAC B.

Table 12: Mean leaf positioning error (absolute) and SD (both mm) for study duration.

Static PF test								
	Log files				EPID			
	LINAC B		LINAC D		LINAC B		LINAC D	
	<i>X1</i>	<i>X2</i>	<i>X1</i>	<i>X2</i>	<i>X1</i>	<i>X2</i>	<i>X1</i>	<i>X2</i>
Mean	0.012	0.010	0.301	0.309	0.248	0.391	0.359	0.162
SD	0.013	0.009	0.036	0.033	0.050	0.035	0.074	0.055
4-field-box								
	Log files							
	LINAC B		LINAC D					
	<i>X1</i>	<i>X2</i>	<i>X1</i>	<i>X2</i>				
Mean	0.115	0.119	0.296	0.291				
SD	0.024	0.024	0.045	0.041				

also the EPID result for LINAC D - *X2* - static PF test: 0.162 mm. In comparison to Tab. 8, the errors listed in Tab. 12 show values for leaf banks *X1* and *X2* of a single LINAC that are more matching in terms of the order of magnitude.

3.1.4 Mean measurement leaf error

Whereas Fig. 24 depicts the mean measurement bank error (average of mean measurement leaf errors over all leaves) vs. time for the static PF test at LINAC D, Fig. 30 concentrates on one particular leaf of bank *X1*, namely leaf no. 21, and shows the development of its mean measurement leaf error in time, derived from log file and EPID data. This is supposed to be an example for a single leaf behaviour.

3.2 Additional tests

3.2.1 Dynamic PF test

Figures 31 and 32 show typical EPID images (LINAC B and LINAC D) acquired for the original as well as the manipulated dynamic PF test irradiations. From the images on the right hand side, it is apparent that a wider gap between two opposing leaves results in a more blackened rectangle and vice versa. This fact, already identifiable with the eye, was verified by the quantitative evaluation with

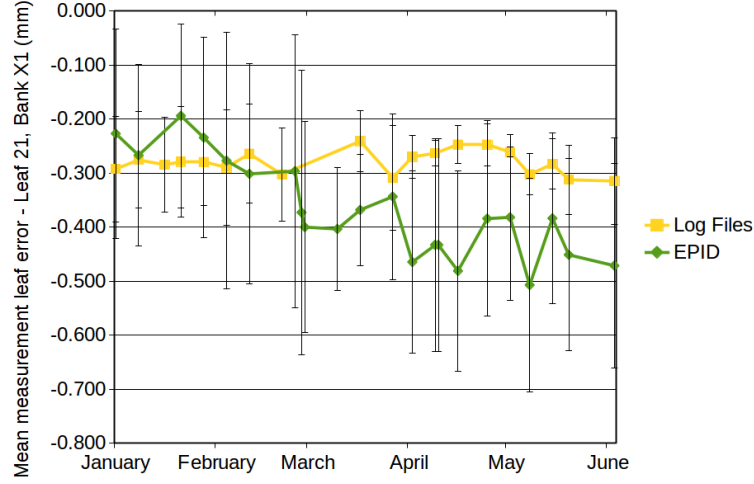


Figure 30: Mean measurement leaf error (mm) ± 1 SD vs. time for static PF test at LINAC D, leaf no. 21, bank X1.

ImageJ (see a screenshot of the program in Fig. 33).

The results of the evaluation are presented in Fig. 34 (for LINAC B) and Fig. 35 (LINAC D). The lower curves depict irradiations of the manipulated plan **c** (e. g. in week 17: w17 c) and their **mean gray value of line read-out** across the MLC banks. From left to right, the peaks reflect the larger or smaller gaps introduced in the dynamic test plan. 2 and 1 mm shifts of leaves were detected with statistical significance (≥ 2 SDs) in terms of comparison with the unmanipulated leaves of the test plan. The gaps which were 0.5 mm larger, too. However, this was not the case for the gaps that were 0.5 mm smaller (≈ 1.2 SDs). On a side note, the SDs in units of mean gray value of line read-out were 419 for LINAC B and 424 for LINAC D, on average. As the upper curves are the results of the original plan (e. g. irradiation in week 15: w15), the graph is quite revealing, because it shows that there is an offset for erroneous irradiations. Now if the “background”, based on the measurements with the unmodified plan, is subtracted, the smallest peak (gap 0.5 mm smaller) also becomes statistically significant for LINAC B and for LINAC D (both ≈ 5 SDs) with SDs in units of mean gray value of line read-out of 184 for LINAC B and 179 for LINAC D, on average. Table 13 shows the details for the significance (in units of SD) obtained on both LINACs. Figures 36 and 37 present the resulting graph when modified and unmodified curves for the certain

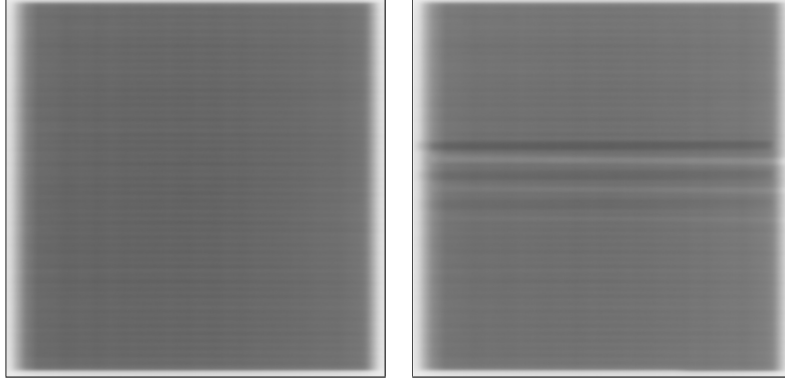


Figure 31: Typical images acquired for dynamic PF tests on LINAC B: Result of original (left) and manipulated (right) plan **c** irradiation.

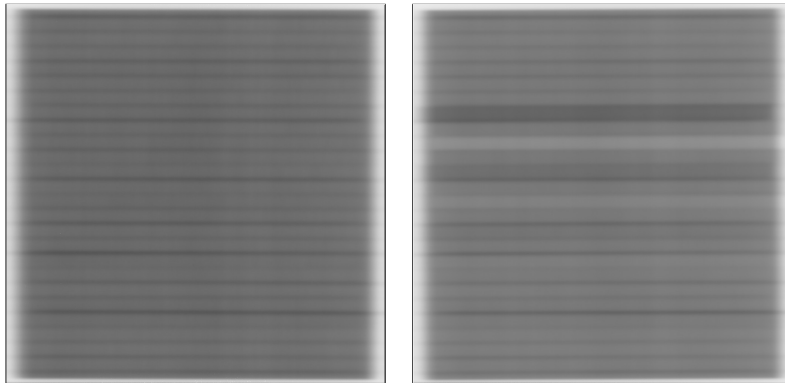


Figure 32: Typical images acquired for dynamic PF tests on LINAC D: Result of original (left) and manipulated (right) plan **c** irradiation.

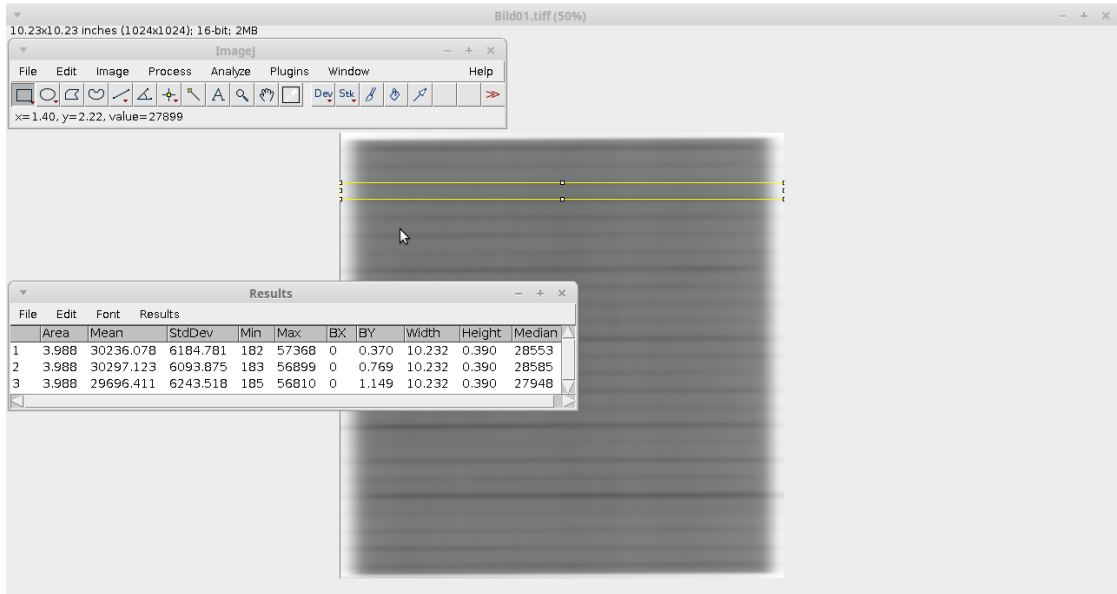


Figure 33: Screenshot of ImageJ: Subsequently, every rectangular representation of the gap between two opposing leaves is measured in terms of mean gray value; the pixel located below the mouse cursor, for example, has a gray value of 27,899.

measurements are averaged prior to the subtraction.

In addition, the dynamic PF test plan was irradiated onto the Delta⁴ phantom (LINAC B). Yet the results seemed not reasonable: *DD*: 1.5% within acceptance criterion, -7.3% Median, *DTA*: 0.0% within criterion, *GPR*: 3.9%.

Table 13: Significance (in units of SD) in detecting leaf errors using the dynamic PF test.

	LINAC B		LINAC D	
	<i>X</i> 1	<i>X</i> 2	<i>X</i> 1	<i>X</i> 2
-0.5 mm	4.9	5.0	5.0	5.5
-1.0 mm	10.3	10.3	11.3	11.0
-2.0 mm	19.9	19.9	22.6	23.0

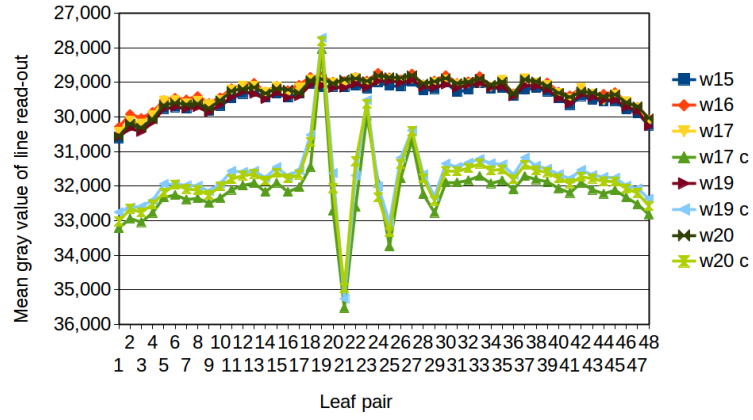


Figure 34: Mean gray value of line read-out (blackening) for dynamic PF tests on LINAC B: Upper curves - original plan, lower curves - manipulated plan **c**.

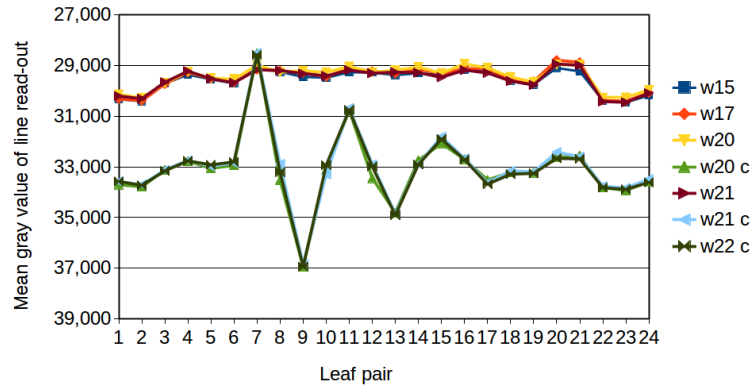


Figure 35: Mean gray value of line read-out (blackening) for dynamic PF tests on LINAC D: Upper curves - original plan, lower curves - manipulated plan **c**.

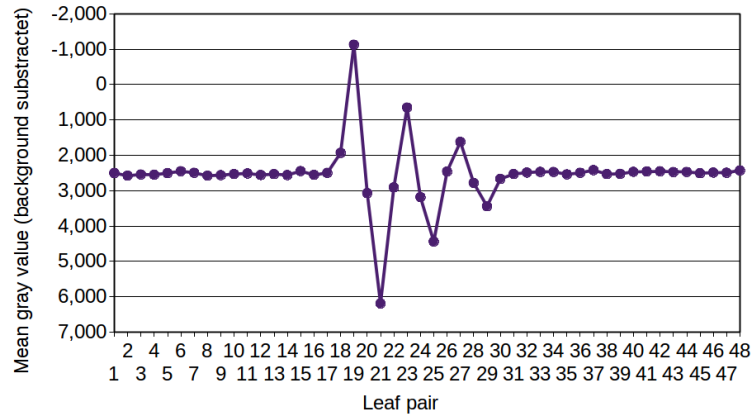


Figure 36: Mean gray value of line read-out for dynamic PF tests on LINAC B: Original plan results (“background”) subtracted from manipulated plan c results.

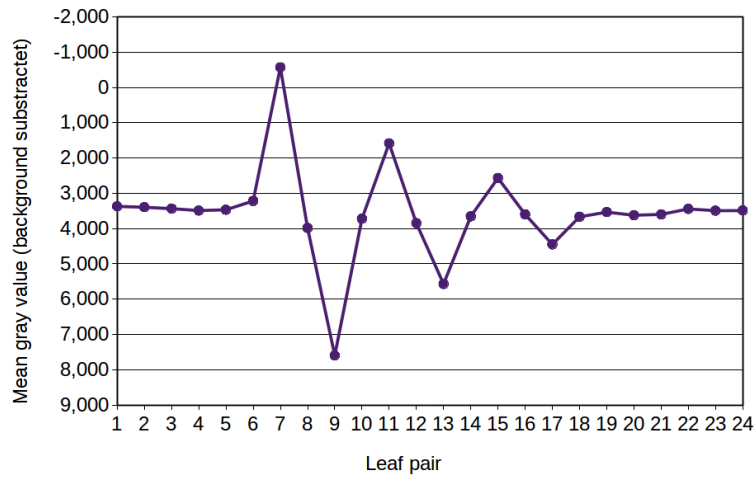


Figure 37: Mean gray value of line read-out for dynamic PF tests on LINAC D: Original plan results (“background”) subtracted from manipulated plan c results.

Table 14: Average of mean measurement bank errors and supposed displacements due to gravity (both mm).

Static PF test (gantry at 0°)								
	Log files				EPID			
	LINAC B		LINAC D		LINAC B		LINAC D	
	X1	X2	X1	X2	X1	X2	X1	X2
Average	0.010	-0.001	-0.304	0.310	0.025	0.197	-0.191	0.008
Gantry at -90°								
	Log files				EPID			
	LINAC B		LINAC D		LINAC B		LINAC D	
	X1	X2	X1	X2	X1	X2	X1	X2
Average	-0.060	-0.088	-0.459	0.297	-0.136	0.187	-0.214	0.055
Displacem.	-0.070	-0.087	-0.155	-0.013	-0.161	-0.010	-0.023	0.047
Gantry at +90°								
	Log files				EPID			
	LINAC B		LINAC D		LINAC B		LINAC D	
	X1	X2	X1	X2	X1	X2	X1	X2
Average	0.091	0.077	-0.300	0.358	-0.113	0.226	-0.387	-0.172
Displacem.	0.081	0.078	0.004	0.048	-0.138	0.029	-0.196	-0.180

3.2.2 Analysis of the influence of gravity

Table 14 lists the average of the mean measurement bank errors of the static PF test irradiations (gantry at 0°) that were the starting point for this analysis. Also the values when rotated to -90° and +90° are given. In addition, the supposed displacements are calculated as the deviation from the error at the unaltered gantry angle. Only for one LINAC and measurement method, surprisingly, a significant result was found (significance in terms of the algebraic sign in accordance to the ground direction and a similar absolute value of the two displacements of the altered gantry positions): log files from the test on LINAC B appeared to show the influence of gravity on the MLC leaves with a systematic displacement of about 0.08 mm on average, in direction to the ground, registered for every bank and position. Figures 38 (bank X1) and 39 (bank X2) visualise this result. The weekly performed measurements are denoted in the legends by “w” and number of week, -/+ stands for -90°/+90°.

Besides, EPID results on LINAC B, bank X2 showed interesting-looking dis-

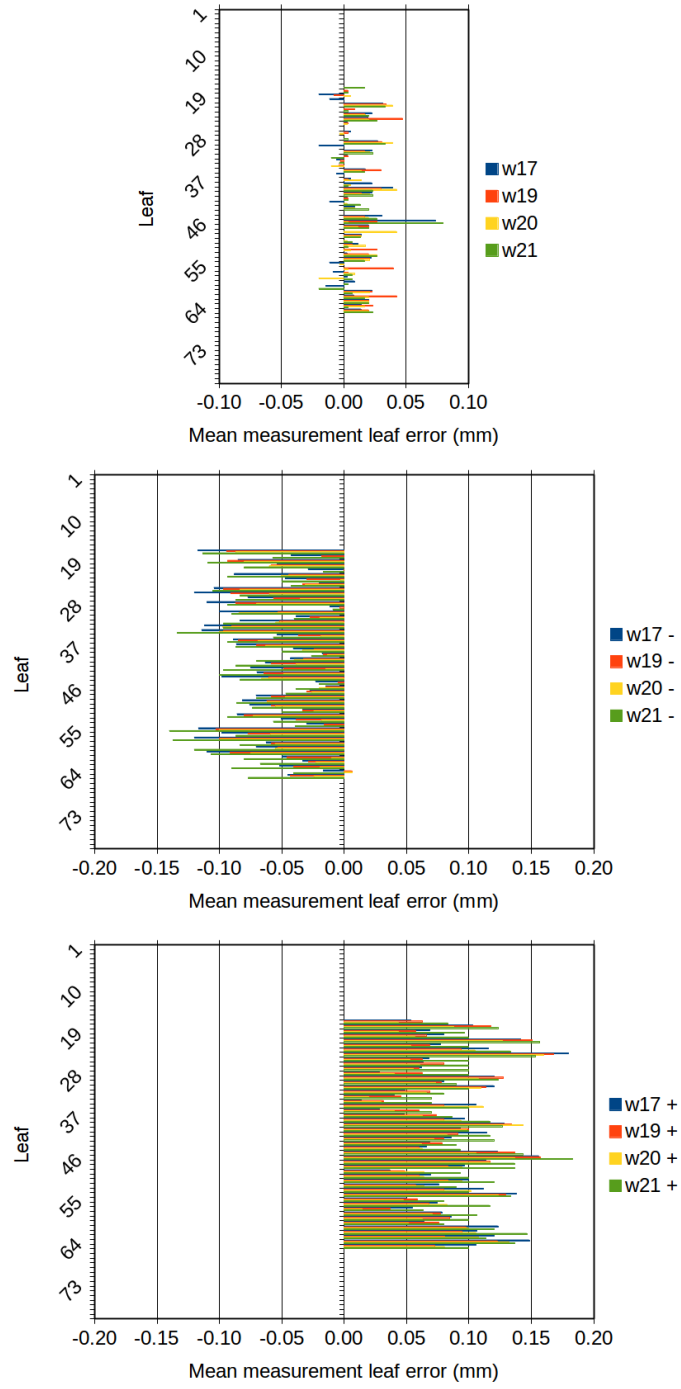


Figure 38: Comparison of static PF test at 0° , -90° and $+90^\circ$ (from top to bottom), LINAC B, bank X1, calculated from log file data.

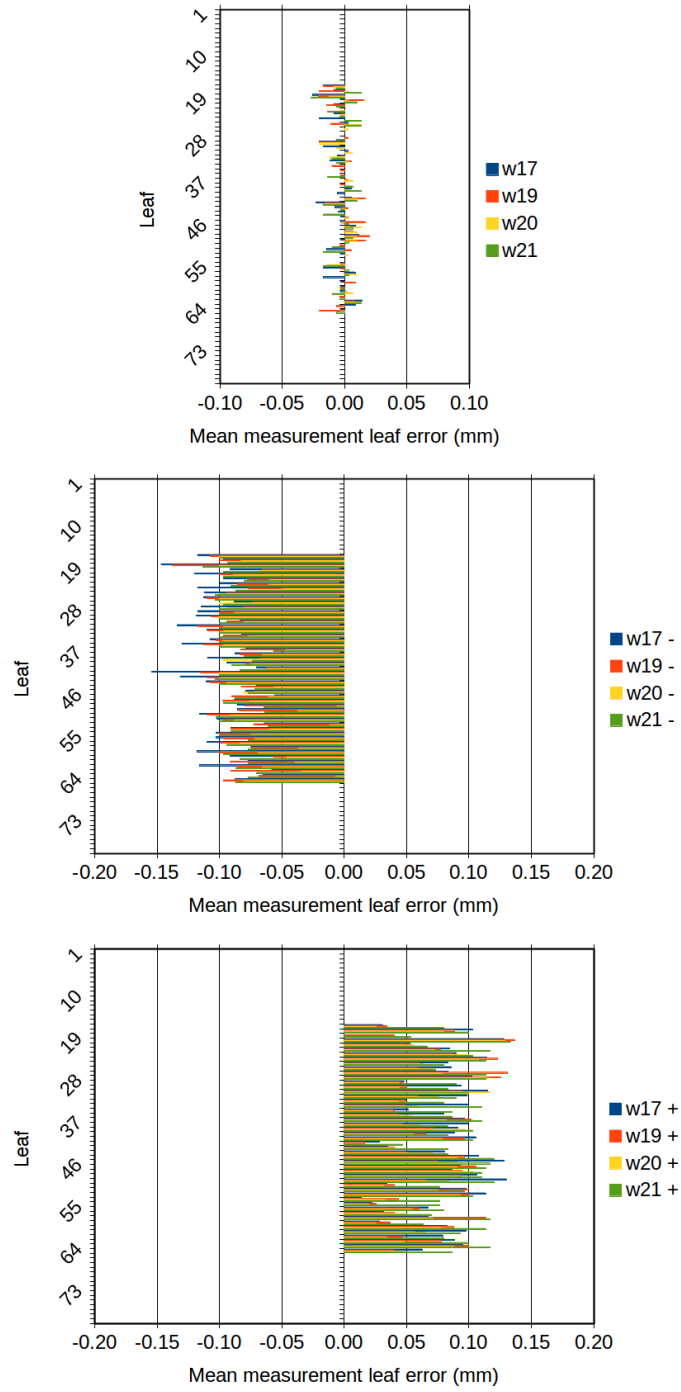


Figure 39: Comparison of static PF test at 0° , -90° and $+90^\circ$ (from top to bottom), LINAC B, bank X2, calculated from log file data.

Table 15: Significance (in units of SD) in detecting leaf errors using the manipulated static PF test.

	LINAC B		LINAC D	
	X1	X2	X1	X2
-0.5 mm	2.0	4.9	4.4	3.1
-1.0 mm	4.9	8.4	8.9	6.8
-2.0 mm	11.2	20.0	15.1	13.0

placements (algebraic sign in accordance to the ground direction) of $-0.010/+0.029$ mm and log file results on LINAC D, also bank X2 $-0.013/+0.048$ mm, for the two altered gantry positions (see Tab. 14). However, the absolute values of the displacements were rather differing from one position to the other. Moreover, a consistent counterpart for the opposing bank was missing.

3.3 Sensitivity analysis

The log files as well as the EPID measurements were able to detect all the introduced leaf positioning errors of 0.5, 1 and 2 mm in the static PF test plan **c**. Tab. 15 shows the significance (in units of SD) for the EPID, which was substantially higher than for the log files. In Fig. 40 the log file based results for LINAC B are diagrammed, Fig. 41 depicts LINAC D. EPID based results can be seen in Fig. 42 (LINAC B) and Fig. 43 (LINAC D). The weekly performed measurements are again denoted in the legends by “w” and number of week, “c” stands for the test plan. The introduced negative errors are evident on both MLC banks.

The sensitivity analysis of the Delta⁴ measurements was less satisfying. Tables 16, 17, 18 and 19 show the results for the test plans **a** and **b** on LINAC B and D, respectively. The measurement dates are denoted by their respective week. For each week, the first line contains the results for the original plan delivered onto the Delta⁴ phantom. By comparison, lines with **a1/b1**, **a2/b2** and **a3/b3** provide the results for the erroneous irradiations (3 steps of shifting the leaves). In any case, the original plan is taken as a basis for the evaluation of the dose

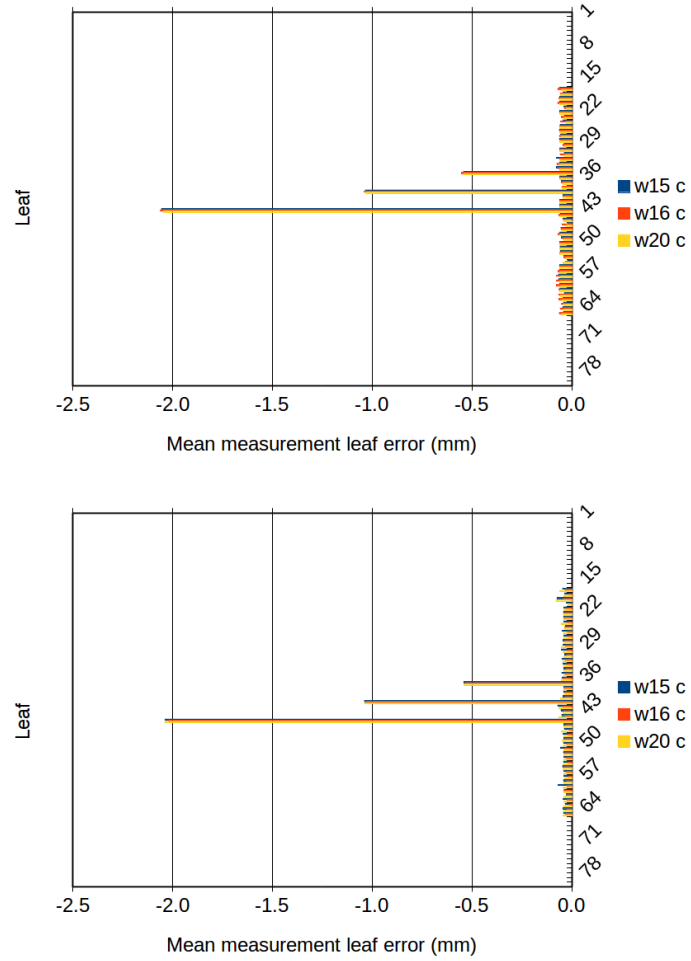


Figure 40: Log file based leaf displacements for static PF test plan **c** on LINAC B, bank *X1* (top) and *X2* (bottom): The introduced negative errors of 0.5, 1 and 2 mm are evident.

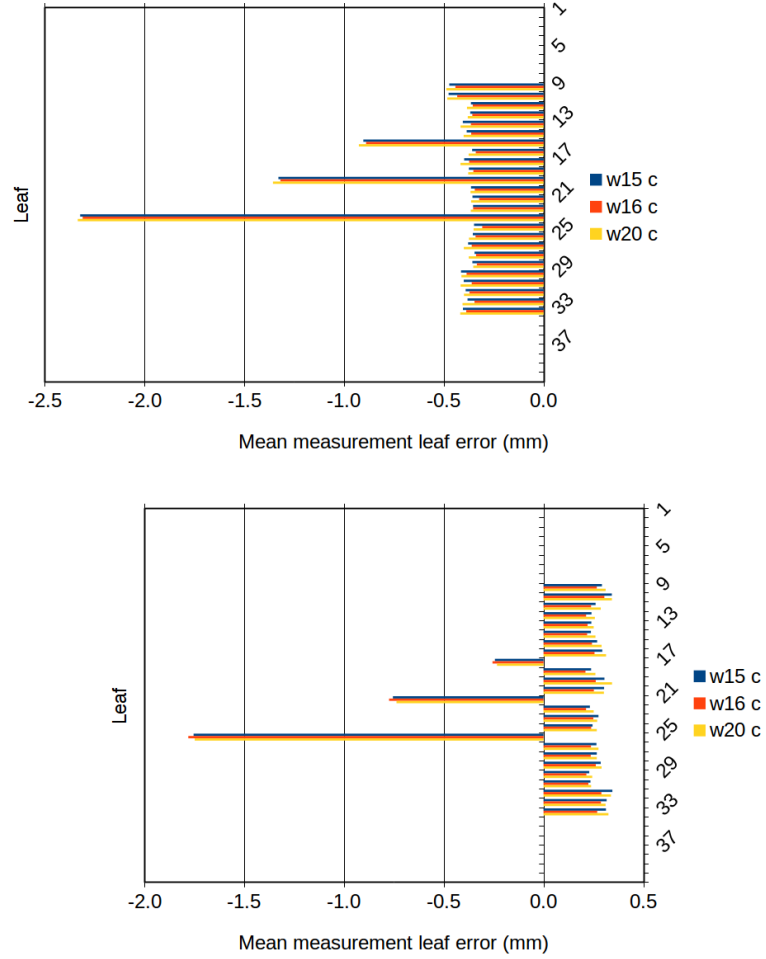


Figure 41: Log file based leaf displacements for static PF test plan **c** on LINAC D, bank X1 (top) and X2 (bottom).

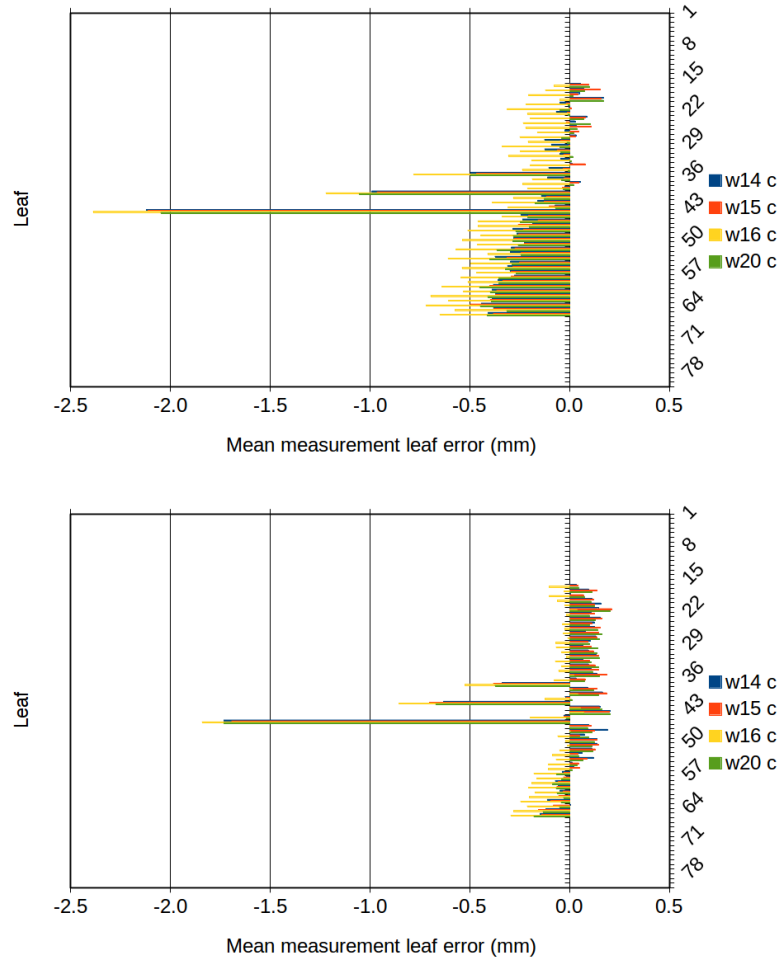


Figure 42: EPID based leaf displacements for static PF test plan **c** on LINAC B, bank X1 (top) and X2 (bottom).

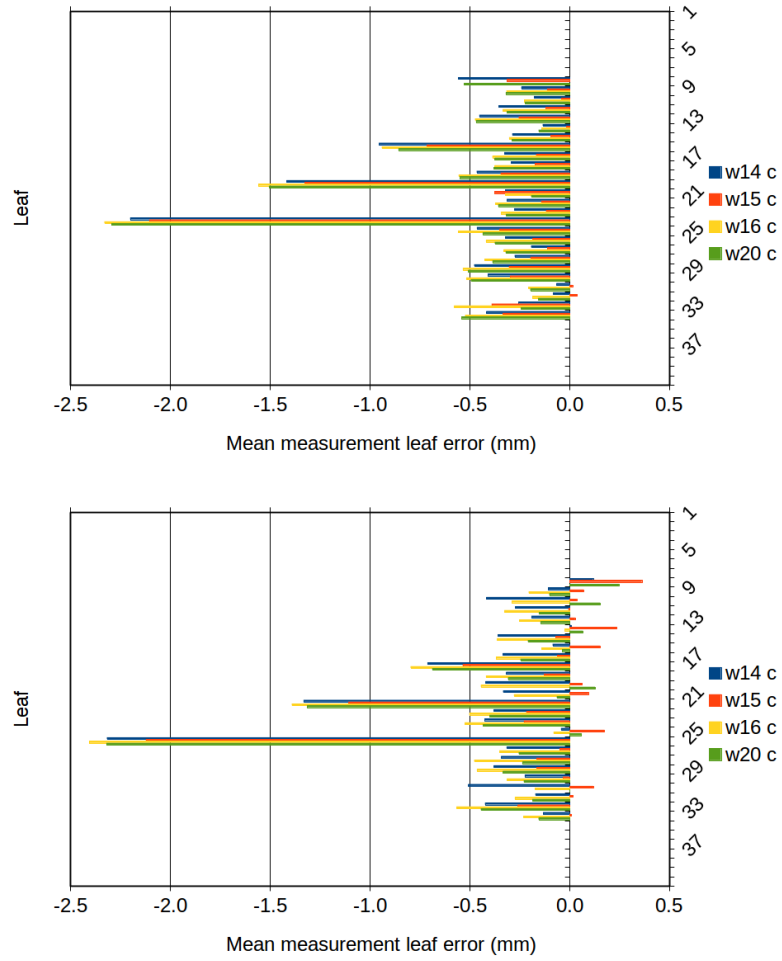


Figure 43: EPID based leaf displacements for static PF test plan **c** on LINAC D, bank X1 (top) and X2 (bottom).

Table 16: Sensitivity analysis of Delta⁴ phantom for LINAC B: Original plan and test plans **a**.

Week	Del.	<i>DD</i> (%)	Med. <i>DD</i> (%)	<i>DTA</i> (%)	<i>GPR</i> (%)
21		9.7	-4.1	100.0	83.1
	a1	26.2	-2.5	100.0	88.4
	a2	13.2	-1.8	100.0	90.1
	a3	13.8	3.2	90.4	85.9
22		12.7	-4.1	100.0	83.9
	a1	20.6	-2.3	100.0	88.8
	a2	12.9	-1.6	100.0	89.9
	a3	13.4	3.3	90.4	85.9
27		15.7	-3.9	100.0	83.5
	a1	20.6	-2.7	100.0	87.6
	a2	12.5	-1.2	99.3	90.6
	a3	13.4	2.8	87.9	83.0

distribution.²² Table 19 is divided into two parts with similar results. Regarding the dose deviation *DD*, significant changes (>2 SDs) from the original plan to the test plan are highlighted in bold. The SDs of the original plan results were: 3.0% for LINAC B - plan **a** (Tab. 16), 3.0% for LINAC B - plan **b** (Tab. 17), 2.0% for LINAC D - plan **a** (Tab. 18) and 0.4% (upper part of Tab. 19) or 6.0% (lower part of Tab. 19) for LINAC D - plan **b**. “Med.” stands for the median (of *DD*). An overall view of the two LINACs and their capability of detecting the artificial leaf errors is given in Tab. 20. It illustrates the mixed outcome: on LINAC D only a shift of 0.5 mm in plan **b** was not identified significantly. On the contrary, on LINAC B only a shift of 0.5 mm in plan **a** could be detected. However, especially the results for LINAC B are questionable.

A second approach for evaluating these data via ScandiDos Delta4 was to compare the Delta⁴ dose measurements of the manipulated plans with the measured dose of the original plan set as reference. Indeed, for LINAC B the step from **a1/b1** to **a2/b2** as well as to **a3/b3** could be detected with statistical significance. This was also true for LINAC D and plans **a**. Unfortunately, data for **b** were not available anymore for later evaluations. Tables 21 and 22 list the re-

²² Also irradiations of the original plan with ScandiDos Delta4 expecting an erroneous plan were tried out, however, did not lead to new information or better statistical significances.

Table 17: Sensitivity analysis of Delta⁴ phantom for LINAC B: Original plan and test plans **b**.

Week	Del.	<i>DD</i> (%)	Med. <i>DD</i> (%)	<i>DTA</i> (%)	<i>GPR</i> (%)
21		9.7	-4.1	100.0	83.1
	b1	13.5	-3.8	100.0	85.8
	b2	15.4	-3.5	100.0	87.3
	b3	9.5	-2.8	98.6	89.4
22		12.7	-4.1	100.0	83.9
	b1	16.5	-3.5	100.0	87.6
	b2	14.6	-3.3	100.0	87.6
	b3	11.7	-2.6	98.2	87.6
27		15.7	-3.9	100.0	83.5
	b1	18.4	-3.5	100.0	86.1
	b2	14.2	-3.4	100.0	86.9
	b3	12.9	-2.7	97.5	85.7

Table 18: Sensitivity analysis of Delta⁴ phantom for LINAC D: Original plan and test plans **a**.

Week	Del.	<i>DD</i> (%)	Med. <i>DD</i> (%)	<i>DTA</i> (%)	<i>GPR</i> (%)
20		14.7	-4.0	100.0	96.1
	a1	23.8	-3.3	100.0	98.9
	a2	46.4	-2.1	100.0	100.0
	a3	37.0	3.5	100.0	100.0
21		10.8	-4.6	100.0	95.9
	a1	17.2	-3.8	100.0	97.4
	a2	49.6	-1.4	100.0	98.5
	a3	28.5	3.8	100.0	100.0
22		13.0	-4.6	100.0	94.2
	a1	20.2	-3.8	100.0	96.8
	a2	36.8	-2.2	100.0	98.9
	a3	35.2	3.1	100.0	100.0

Table 19: Sensitivity analysis of Delta⁴ phantom for LINAC D: Original plan and test plans **b**.

Week	Del.	<i>DD</i> (%)	Med. <i>DD</i> (%)	<i>DTA</i> (%)	<i>GPR</i> (%)
13		46.6	-2.8	100.0	98.5
	b1	45.2	-2.2	100.0	99.6
	b2	39.8	-1.9	100.0	99.6
	b3	38.2	-1.5	100.0	100.0
14		47.2	-3.1	100.0	98.1
	b1	48.1	-2.5	100.0	98.9
	b2	42.9	-2.4	100.0	99.3
	b3	39.7	-1.7	100.0	100.0
15		0.0	-84.9	0.0	0.0
	b1	18.1	-3.8	100.0	99.6
	b2	28.5	-3.2	100.0	99.6
	b3	33.5	-2.7	100.0	100.0
16		23.6	-4.5	100.0	97.8
	b1	29.1	-3.9	100.0	97.8
	b2	32.5	-3.4	100.0	98.1
	b3	33.1	-2.9	100.0	99.3
17		13.5	-4.6	100.0	98.1
	b1	25.5	-3.7	100.0	99.3
	b2	31.1	-3.3	100.0	99.6
	b3	31.8	-2.7	100.0	100.0
19		12.9	-4.3	100.0	97.8
	b1	13.2	-4.2	100.0	98.2
	b2	18.3	-3.8	100.0	97.8
	b3	23.8	-3.3	100.0	98.2

Table 20: Sensitivity analysis of Delta⁴ phantom, overall.

	a			b		
	1	2	3	1	2	3
LINAC B	yes	no	no	no	no	no
LINAC D	yes	yes	yes	no	yes	yes

Table 21: Sensitivity analysis of Delta⁴ phantom for LINAC B: Original plan (set as reference) and test plans **a**.

Week	Del.	<i>DD</i> (%)	Med. <i>DD</i> (%)	<i>DTA</i> (%)	<i>GPR</i> (%)
21		100.0	0.0	100.0	100.0
	a1	59.9	0.5	100.0	90.6
	a2	55.9	0.9	83.4	90.6
	a3	48	2.6	67.2	72.7
22		100.0	0.0	100.0	100.0
	a1	59.7	0.6	100.0	89.9
	a2	55.4	1	83.4	90.7
	a3	48	2.7	66.8	72.2
27		100.0	0.0	100.0	100.0
	a1	66.3	1.5	100.0	98.9
	a2	47.9	2.1	92.8	90.7
	a3	41.8	2.7	67.2	72.2

sults for LINAC B, original plan and test plans **a** and **b**, respectively. Table 23 summarises the updated overall result.

3.4 Gun current

The electron gun current was one of the additional parameters recorded via the LINAC log files. Nevertheless, a striking result was revealed: Gun current declined over six months by 0.08 mA at LINAC B and 0.22 mA at LINAC D, respectively. As depicted in Fig. 44, the drop was consistently discovered for all major test plans. A linear fit is drawn and its equation printed above the curves. x is to be understood in unit of days with the first measurement starting at day 0. The coefficients of determination R^2 are high, 0.95 on average, i. e. the measured values are located close to the linear slope. Intercept and slope were considered as the estimated values $\hat{\alpha}$ and $\hat{\beta}$, respectively. Table 24 displays the test parameter $T = |\hat{\beta}|/\hat{\sigma}_{\hat{\beta}}$ ($T = |\hat{\alpha}|/\hat{\sigma}_{\hat{\alpha}}$) as well as the critical value $t_{0.975}^{n-2}$ for a 5% level of significance, taken from [19], for all test plans and both LINACs. As depicted, the parameters are high above the critical values (which are 2.132 on average), especially for the intercept. For that reason, a linear relationship between gun current and time can be assumed with high statistical significance.

Table 22: Sensitivity analysis of Delta⁴ phantom for LINAC B: Original plan (set as reference) and test plans **b**.

Week	Del.	<i>DD</i> (%)	Med.	<i>DD</i> (%)	<i>DTA</i> (%)	<i>GPR</i> (%)
21		100.0		0.0	100.0	100.0
	b1	85.4		0.1	100.0	99.6
	b2	78.7		0.2	100.0	96.6
	b3	68.9		0.5	94.2	94.3
22		100.0		0.0	100.0	100.0
	b1	83.5		0.2	100.0	100.0
	b2	79.8		0.3	99.6	96.6
	b3	70.8		0.6	93.4	96.1
27		100.0		0.0	100.0	100.0
	b1	92.9		0.6	100.0	100.0
	b2	81.8		0.7	100.0	98.5
	b3	73.8		1.0	95.3	96.8

Table 23: Sensitivity analysis of Delta⁴ phantom, overall, after second approach.

	a			b		
	1	2	3	1	2	3
LINAC B	yes	yes	yes	no	yes	yes
LINAC D	yes	yes	yes	no	yes	yes

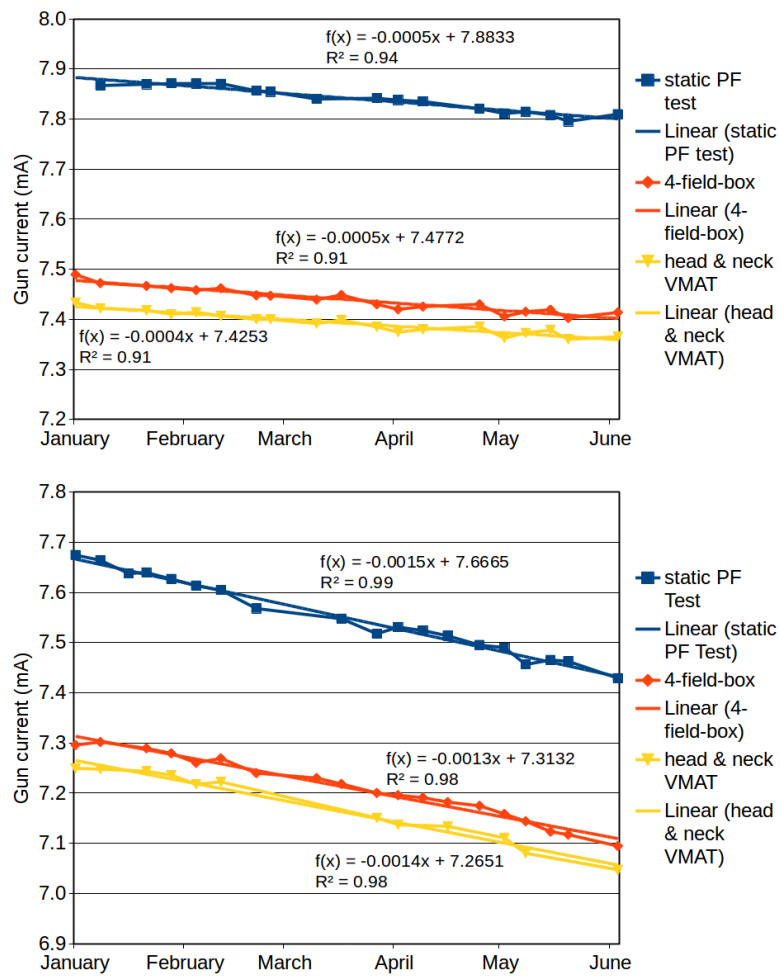


Figure 44: Gun current (mA) over time: LINAC B (top) and LINAC D (bottom).

Table 24: Linear regression model for electron gun current: t-test of regression coefficients α and β .

Static PF test				
	LINAC B		LINAC D	
	α	β	α	β
T	2343.466	14.822	1901.014	34.136
$t_{0.975}^{n-2}$	2.131	2.131	2.110	2.110
4-field-box				
	LINAC B		LINAC D	
	α	β	α	β
T	2244.037	13.150	1755.391	29.058
$t_{0.975}^{n-2}$	2.110	2.110	2.101	2.101
Head & neck VMAT				
	LINAC B		LINAC D	
	α	β	α	β
T	2606.241	13.458	1450.739	22.874
$t_{0.975}^{n-2}$	2.110	2.110	2.228	2.228

4 Discussion

Recording the log files in the LINAC's service mode worked smoothly except for the VMAT irradiations on LINAC D, where 7 out of 19 files were corrupt. In total, 576 log files could be recorded and evaluated.

4.1 Static PF test, consistency checks

The mean leaf errors and their derived quantities (mm) were obtained from the MLC log files/`LogAnalyzer` with up to 9 digits. Although measurements with the EPID panel/`MLC Soft EPID` do not provide this precision, 3 significant digits (micrometres) were used.

According to the log file data, the **mean leaf positioning error** was found to be different between LINAC D and B (see Tab. 8). This could be explained by the different optical MLC leaf position measurement techniques used by the treatment heads MLCi2 and Agility: Visible light vs. ultraviolet/infrared (compare Sec. 2.1.1).

Another interesting finding were the symmetrical **mean measurement bank**

errors and consequently symmetrical mean leaf positioning errors of the banks of LINAC D (symmetrical around 0, see also Fig. 22). As a matter of fact, this pattern may be calibrated by the manufacturer as a leaf crash prevention feature. However, the gap of about 0.6 mm was still below the limit of 1 mm for the field size, accepted in clinical routine and according to standards.

The **SD** was higher for the VMAT plan than for the static plans, presumably because the leaves were moving during the irradiation (and therefore measurement) process. Higher values of SD were obtained by the EPID, too. This may be due to the finite resolution of the EPID panel with its pixel size of 0.4 mm.

As mentioned in the literature review (Sec. 1.6), Agnew et al. [28] found a positional leaf error of 0.004 ± 0.011 mm on Varian machines, delivering a static PF test and using log files. In this thesis, LINAC B, especially MLC bank X2, showed a quite similar result with -0.002 ± 0.010 mm. Besides, also the larger SDs for the EPID were consistent.

Again on LINAC B, mean leaf positioning error and SD for the VMAT were in the same order of magnitude (precisely -0.159 ± 0.121 mm X1, -0.207 ± 0.139 mm X2) as in the multi-institutional study by Pasler et al. [37] (0.3 ± 0.2 mm for log files from Elekta LINACs).

Only a poor **correlation** could be found between log file and EPID/Delta⁴ data for the 4-field-box ($r \sim 0.31$) and the static PF test (0.27). Almost no correlation (0.06) was obtained for the head & neck VMAT. Due to this discrepancy, the calibration of the MLC has to be performed and monitored via a LINAC-independent measurement system.

Comparing the development of the **SD of the mean measurement bank error** over time to the development of the *GPR* at LINAC B for the VMAT and 4-field-box irradiation (Fig. 28 and 29), one can state that the system was running rather stable. The same holds true for LINAC D. Then again, it could also be that the SD of the log files does not change with time at all.

Using the mean of the **absolute** values of the mean leaf errors for calculating the mean measurement leaf error and subsequently the **mean leaf positioning error** (Tab. 12) may come with the advantage that positive and negative errors (with

same absolute values) do not average each other out. On the other hand, such errors (consecutive over- and undershoot of the same magnitude) would probably have no effect on the total dose delivered, only on the spatial distribution. Since the banks $X1$ and $X2$ of LINAC D showed the pattern of a slightly larger field for the static PF test and 4-field-box, mean measurement bank errors were always distinctly positive or negative. As a result, absolute values were the same when calculating mean of absolute values. In contrast, errors on LINAC B would have been underestimated when solely relying on the mean of mean leaf errors. Besides, also RMS errors (compare Eq. 28 in Sec. 2.3) are applied in some studies found in the literature, e.g. Defoor et al. [36] or Kabat et al. [39]. As with the mean of absolute values, positive and negative values do not average each other out because of the squaring down. However, outliers could distort the result.

Mean measurement leaf error of leaf no. 21 (bank $X1$, LINAC D, static PF test), Fig. 30, resembles the development of the mean measurement bank error, Fig. 24, derived from it.

4.2 Additional tests

4.2.1 Dynamic PF test

The images on the left side of Fig. 31 and 32 confirm the anticipated result of Fig. 19, Sec. 2.6.1.

The fact that there was an offset between the original and the manipulated dynamic PF test plan, in terms of mean gray value of line read-out (Fig. 34 and 35), may not be a physical phenomenon but rather a result of the image generation by the EPID system. Nonetheless, a dynamic PF test may be useful in quality assurance to monitor the MLC leaf calibration, except that it is probably not possible to discriminate between the two MLC banks. Comparing with the sensitivity analysis using the static PF test (Tab. 15), the significance in detecting leaf errors was slightly higher (Tab. 13).

Irradiating the test plan onto the Delta⁴ phantom did not lead to useful results. Maybe because the two CPs lay outside of the cylindrical phantom in the frontal plane and dose calculation was not possible due to that.

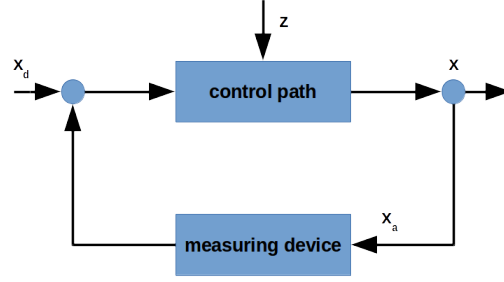


Figure 45: Simplified scheme of a control loop as background of the MLC’s leaf position control system.

4.2.2 Analysis of the influence of gravity

Little movement of the MLC leaves due to the gravitational force is to be expected when rotating the gantry to the positions of minus or plus 90° . One has to consider loose fit of some mechanical parts. Interestingly, such a systematic displacement was only found for LINAC B (log file data from static PF test). An explanation for this could be the additional mechanics, in form of the dynamic leaf guide, which is installed in the Agility treatment head. Another reasonable explanation for a displacement of 0.08 mm might be that the LINAC has a threshold (“leaf control parameter”) of about 0.1 mm, before it starts correcting positioning errors. Figure 45 shows the simplified scheme of a control loop. x denotes the control variable, x_a its actual value and x_d its desired value. In this case, the leaf position represents the control variable, which is measured and compared with the desired value. Differences are caused by the disturbing variable z (gravitational force). They may be tolerated if not exceeding a certain threshold. Otherwise, the leaf position will be readjusted. In this analysis of the influence of gravity on the MLC leaves, the systematic displacement found on LINAC B may have stayed below such a threshold or the control system moved the leaves below the threshold.

4.3 Sensitivity analysis

Evaluating the sensitivity checks, statistical significance for the detection of introduced leaf errors was assumed for greater than or equal 2 SDs above the mean measurement bank error (only unmanipulated leaves considered). However, especially on LINAC B (small mean leaf positioning error derived from log files), the significance was much higher (around 40 to 220 SDs), presumably due to the Rubicon optical technology.

In comparison, the intentional displacement of -0.5 mm on LINAC B, bank *X1* would almost not have been detected significantly via the EPID if not known as an error (compare top of Fig. 42). For three of four measurements, the corresponding mean measurement leaf error was in the same range as the “noise”. Furthermore, the diagonal pattern visible is not likely to reflect a sag of the EPID panel, as could be suspected, because it lacks its counterpart in the results for bank *X2*.

Unexpectedly, regarding the sensitivity analysis of the Delta⁴ phantom, *GPR* was increasing, the more erroneous the test plans became (in some cases dropped again for larger leaf errors). This was also found for *DD* and Med. *DD*, and could be explained by uncertainty of dose calculation due to small fields. For this reason, the second approach was started. As depicted in Tab. 21 and 22, eventually, the expected behaviour of declining *DD* and *GPR* could be observed. As summarised in Tab. 23, the Delta⁴ phantom was not capable of detecting a 0.5 mm manipulation of every third leaf (plan **b**) of a bank.

As the log files were able to detect artificially introduced leaf errors, it can be assumed that this technology is capable of discovering substantial positioning errors when delivering a patient treatment (of course, also the fact that a wrong treatment plan is transmitted to the LINAC). Comparison between log file and plan file has to be automated and conducted immediately after irradiation. This would allow for machine as well as patient specific quality assurance. Before clinical use, a further study applying the LINAC’s clinical mode is suggested. Certain differences between service and clinical mode of the machine, in terms of performance, may exist. Future work could also contain a dose recalculation for patient specific

QA as described by Tyagi et al. [32] or Stanhope et al. [40].

4.4 Gun current

A possible explanation for the decrease of gun current over time might be the release of material from the cathode. According to Ohm's law,

$$V = R I \quad (32)$$

for a constant acceleration voltage V (V) between cathode and anode, a decrease in current I (A) must be caused by an increase in resistance R (Ω). The latter can be described by a loss of the cross-sectional area A (cm^2) through

$$R = \frac{\rho l}{A} \quad (33)$$

with l (cm) being the length of the conductor and ρ (Ωcm) the specific electrical resistance. Moreover, heat stress could lead to deformations of the spiral-shaped tungsten wire and contacts between adjacent sections may emerge.

From time to time, the medical LINAC's electron gun fails. As a result, the machine is down for maintenance, unavailable for the clinical operation.²³ In a further study, it should be continued to log the gun current so as to eventually encounter a breakdown of the gun and find a numerical value of decrease for a possible future prediction of these instances. Of course, field engineers already monitor the gun current, but not the trend over time.

²³ Especially the reestablishment of the vacuum, after changing the gun, is time-consuming.

5 Conclusions

On the one hand, it was possible to detect artificially introduced leaf errors via the log files. On the other hand, the time development of the mean measurement bank error did not correlate with the behaviour monitored by the EPID and the Delta⁴ phantom on a long time basis. The log files did not reproduce the system adequately – as seen from independent measurements. However, given that the leaves are calibrated optimally, which is to be monitored via an independent measurement system, MLC log files seem to detect positional errors in the treatment delivery.

In conclusion, log files appear to be able to provide a variety of useful data for every treatment delivery performed, e. g. influence of gravity on the MLC leaves or decrease in gun current. Log files might have the potential to act as an additional QA procedure. Moreover, the fact that the data is gathered on-line, during the treatment delivery, offers higher efficiency, because it spares dedicated machine time for QA, and, if necessary, makes it possible to take action earlier.

Acronyms

BEV beam's eye view

CIP continuous improvement process

CP control point

CRT conformal radiation therapy

CT computed tomography

CTV clinical target volume

DNA deoxyribonucleic acid

DVH dose-volume-histogram

EPID electronic portal imaging device

FOV field of view

FWHM full width half maximum

GTV gross tumour volume

IDM intelligent device management

IGRT image-guided radiation therapy

IMAT intensity-modulated arc therapy

IMRT intensity-modulated radiation therapy

ITV internal target volume

LAN local area network

LINAC linear accelerator

MLC multi leaf collimator

MRI magnetic resonance imaging

MU monitor unit

OAR organs at risk

PF picket fence

PMMA polymethylmethacrylate

PTV planning target volume

QA quality assurance

QM quality management

RMS root mean square

ROI region of interest

SAD source to axis distance

SBRT stereotactic body radiation therapy

SD standard deviation

SRS stereotactic radiosurgery

SSD source to surface distance

TPS treatment planning system

VMAT volumetric-modulated arc therapy

List of Figures

1	Relative importance of the three principal interactions of photon beams in matter.	5
2	DNA double helix.	7
3	Block diagram of a typical medical LINAC.	8
4	Magnetron, sectional view.	9
5	Two-cavity klystron.	9
6	Concept of electron acceleration via a travelling wave.	11
7	Concept of electron acceleration via a standing wave.	11
8	Treatment head of medical LINAC, schematic.	11
9	MLC by Varian.	13
10	SAD vs. SSD setup for photon beam calibration.	13
11	Advanced external beam radiotherapy devices by Accuracy.	18
12	Example of dose distribution for a 4-field-box treatment.	20
13	LINACs and treatment rooms.	28
14	ScandiDos Delta ⁴ phantom, schematic.	30
15	Delta ⁴ phantom on treatment couch.	31
16	Geometric representation of gamma index γ	32
17	Screenshot of LogAnalyzer by Andreas Moser, with annotations. . .	35
18	Static PF test sequence.	36
19	Anticipated result for dynamic PF test at LINAC D.	38
20	Screenshot of Oncentra TPS with annotations.	39
21	Test plans for sensitivity checks.	40
22	Mean measurement bank error vs. time for static PF test and 4-field-box at LINAC D.	44
23	Mean measurement bank error vs. time for static PF test at LINAC B.	46
24	Mean measurement bank error vs. time for static PF test at LINAC D.	47
25	Scatter plots for static PF test.	48
26	Scatter plots for 4-field-box.	49
27	Scatter plots for head & neck VMAT.	50
28	SD and GPR vs. time for VMAT at LINAC B.	51
29	SD and GPR vs. time for 4-field-box at LINAC B.	51
30	Mean measurement leaf error vs. time for static PF test at LINAC D, leaf no. 21, bank X1.	53
31	Typical images acquired for dynamic PF tests on LINAC B.	54
32	Typical images acquired for dynamic PF tests on LINAC D.	54
33	Screenshot of ImageJ.	55
34	Mean gray value of line read-out for dynamic PF tests on LINAC B. .	56

35	Mean gray value of line read-out for dynamic PF tests on LINAC D.	56
36	Mean gray value of line read-out (background subtracted) for dynamic PF tests on LINAC B.	57
37	Mean gray value of line read-out (background subtracted) for dynamic PF tests on LINAC D.	57
38	Comparison of static PF test at 0° , -90° and $+90^\circ$, LINAC B, bank X1, calculated from log file data.	59
39	Comparison of static PF test at 0° , -90° and $+90^\circ$, LINAC B, bank X2, calculated from log file data.	60
40	Log file based leaf displacements for static PF test plan c on LINAC B, bank X1 and X2.	62
41	Log file based leaf displacements for static PF test plan c on LINAC D, bank X1 and X2.	63
42	EPID based leaf displacements for static PF test plan c on LINAC B, bank X1 and X2.	64
43	EPID based leaf displacements for static PF test plan c on LINAC D, bank X1 and X2.	65
44	Gun current over time: LINAC B and D.	71
45	Simplified scheme of a control loop as background of the MLC's leaf position control system.	75

List of Tables

1	Literature on LINAC log files.	21
2	Technical overview of Elekta LINACs used.	28
3	Configuring service graphing in LINAC's service mode: items and parts for logging.	33
4	Specifications of the static PF test.	35
5	Acceptance criteria for consistency checks following the concept of γ index.	37
6	Specifications of the dynamic PF test.	37
7	Specifications of sensitivity test plan c.	40
8	Mean leaf positioning error and SD for study duration.	43
9	Pearson correlation coefficients for static PF test.	46
10	Pearson correlation coefficients for 4-field-box.	47
11	Pearson correlation coefficients for head & neck VMAT.	48
12	Mean leaf positioning error (absolute) and SD for study duration.	52
13	Significance in detecting leaf errors using the dynamic PF test.	55
14	Average of mean measurement bank errors and supposed displacements due to gravity.	58
15	Significance in detecting leaf errors using the manipulated static PF test.	61
16	Sensitivity analysis of Delta ⁴ phantom for LINAC B: Original plan and test plans a.	66
17	Sensitivity analysis of Delta ⁴ phantom for LINAC B: Original plan and test plans b.	67
18	Sensitivity analysis of Delta ⁴ phantom for LINAC D: Original plan and test plans a.	67
19	Sensitivity analysis of Delta ⁴ phantom for LINAC D: Original plan and test plans b.	68
20	Sensitivity analysis of Delta ⁴ phantom, overall.	68
21	Sensitivity analysis of Delta ⁴ phantom for LINAC B: Original plan (set as reference) and test plans a.	69
22	Sensitivity analysis of Delta ⁴ phantom for LINAC B: Original plan (set as reference) and test plans b.	70
23	Sensitivity analysis of Delta ⁴ phantom, overall, after second approach.	70
24	Linear regression model for electron gun current: t-test of regression coefficients.	72

References

- [1] P. Mayles, A. Nahum, and J.C. Rosenwald. *Handbook of Radiotherapy Physics: Theory and Practice*. CRC Press, 2007. ISBN 9781420012026.
- [2] E. B. Podgorsak. Radiation oncology physics: A handbook for teachers and students. Technical report, International Atomic Energy Agency, Vienna, July 2005. STI/PUB/1196.
- [3] P. Feyer and A. Buchali. Strahlentherapie: Moderne und individuelle tumorbehandlung. *best practice onkologie*, 5(2):42–55, 2007. German.
- [4] M. Wannemacher, J. Debus, and F. Wenz. *Strahlentherapie*. Springer Berlin Heidelberg, 2006. ISBN 9783540228127. German.
- [5] Dietmar Georg. Radiation oncology physics. lecture slides, June 2015.
- [6] Faiz Khan. *The physics of radiation therapy*. Lippincott Williams and Wilkins, 1994.
- [7] F.H. Attix. *Introduction to Radiological Physics and Radiation Dosimetry*. Wiley, 2008. ISBN 9783527617142.
- [8] Relative importance of the three principal interactions in matter. <http://www.ilocis.org/documents/images/ion01fe.gif>. International Labour Office, accessed February 2016.
- [9] Dna double helix. <http://ghr.nlm.nih.gov/handbook/illustrations/dnastructure.jpg>. U.S. National Library of Medicine, accessed November 2015.
- [10] Hannes Aiginger and Karin Poljanc. Teilchenbeschleuniger. lecture notes, 2005. German.
- [11] Wolfgang Lechner. Intensity modulated radiotherapy using flattening filter free photon beams. Master’s thesis, Vienna University of Technology, November 2011.
- [12] Multi leaf collimator (mlc) by varian. http://filecache.drivetheweb.com/mr5mr_varian/154577/MLC+-+gold.jpg. Accessed July 2015.
- [13] Sad vs. ssd setup. http://images.slideplayer.com/38/10795616/slides/slide_20.jpg. Accessed November 2016.

- [14] Absorbed dose determination in external beam radiotherapy. Technical Report 398, International Atomic Energy Agency, Vienna, December 2000. STI/-DOC/010/398.
- [15] Kilby W, Dooley JR, Kuduvalli G, Sayeh S, and Maurer CR Jr. The cyberknife robotic radiosurgery system in 2010. *Technol. Cancer Res Treat*, 9(5):433–452, October 2010. <http://tct.sagepub.com/content/9/5/433.long>.
- [16] Treatment delivery solutions. <http://www accuray.com/node/42>, . Accuray Inc., accessed February 2016.
- [17] Cyberknife. http://www accuray.com/sites/default/files/vpk_assets/cyberknife_g4_suite.jpg, . Accuray Inc., accessed February 2016.
- [18] Tomotherapy. http://www accuray.com/sites/default/files/vpk_assets/tomo_2669.jpg, . Accuray Inc., accessed February 2016.
- [19] Wolfgang Timischl. *Qualitätssicherung*. Hanser, München, Wien, 3rd edition, 2002. ISBN 3-446-22053-4. German.
- [20] Albrecht Baumann, Arndt Kirchner, Manfred Maier, Gerd Rohde, Gert Robens, and Dietmar Schmid. *Produktionsorganisation*. Bibliothek des technischen Wissens. Europa Lehrmittel, Haan-Gruiten, 2nd edition, 2002. German.
- [21] E. Richter and T. Feyerabend. *Grundlagen der Strahlentherapie*. Springer, 1996. German.
- [22] Eric E. Klein, Joseph Hanley, John Bayouth, Fang-Fang Yin, William Simon, Sean Dresser, Christopher Serago, Francisco Aguirre, Lijun Ma, Bijan Arjomandy, and Chihray Liu. Task group 142 report: Quality assurance of medical accelerators. *Medical Physics*, 36(9):4197–4212, September 2009.
- [23] Sonja Dieterich, Carlo Cavedon, Cynthia F. Chuang, Alan B. Cohen, Jeffrey A. Garrett, Charles L. Lee, Jessica R. Lowenstein, Maximian F. d’Souza, David D. Taylor Jr., Xiaodong Wu, and Cheng Yu. Task group 135 report: Quality assurance for robotic radiosurgery. *Medical Physics*, 38(6):2914–2936, June 2011.
- [24] Katja M. Langen, Niko Papanikolaou, John Balog, Richard Crilly, David Followill, S. Murty Goddu, Walter Grant III, Gustavo Olivera, Chester R. Ramsey, and Chengyu Shi. Task group 148 report: Qa for helical tomotherapy. *Medical Physics*, 37(9):4817–4853, September 2010.

- [25] Gerald J. Kutcher, Lawrence Coia, Michael Gillin, William F. Hanson, Steven Leibel, Robert J. Morton, Jatinder R. Palta, James A. Purdy, Lawrence E. Reinstein, Goran K. Svensson, Mona Weller, and Linda Wingsfield. Comprehensive qa for radiation oncology. Technical Report 46, American Association of Physicists in Medicine by the American Institute of Physics, April 1994.
- [26] Dale W. Litzenberg, Jean M. Moran, and Benedick A Fraass. Verification of dynamic and segmental imrt delivery by dynamic log file analysis. *Journal of Applied Clinical Medical Physics*, 3(2):63–72, 2002. URL <http://www.jacmp.org/index.php/jacmp/article/viewFile/2578/1046>.
- [27] C E Agnew, R B King, A R Hounsell, and C K McGarry. Implementation of phantom-less imrt delivery verification using varian dynalog files and r/v output. *Physics in Medicine and Biology*, 57:6761–6777, 2012. URL <http://iopscience.iop.org/0031-9155/57/21/6761/>.
- [28] A Agnew, C E Agnew, M W D Grattan, A R Hounsell, and C K McGarry. Monitoring daily mlc positional errors using trajectory log files and epid measurements for imrt and vmat deliveries. *Physics in Medicine and Biology*, 59(9):N49–N63, 2014. URL <http://stacks.iop.org/0031-9155/59/i=9/a=N49>.
- [29] James Kerns, Nathan Childress, and Stephen Kry. A multi-institution evaluation of mlc log files and performance in imrt delivery. *Radiation Oncology*, 9(1):176, 2014. ISSN 1748-717X. doi: 10.1186/1748-717X-9-176. URL <http://www.ro-journal.com/content/9/1/176>.
- [30] Jong Min Park, So-Yeon Park, Hyoungnyoun Kim, Jin Ho Kim, Joel Carlson, and Sung-Joon Ye. Modulation indices for volumetric modulated arc therapy. *Physics in Medicine and Biology*, 59(23):7315–7340, 2014. URL <http://stacks.iop.org/0031-9155/59/i=23/a=7315>.
- [31] J M Park, H-G Wu, J H Kim, J N K Carlson, and K Kim. The effect of mlc speed and acceleration on the plan delivery accuracy of vmat. *British Journal of Radiology*, 88, 2015. <http://www.birpublications.org/doi/pdf/10.1259/bjr.20140698>.
- [32] Neelam Tyagi, Kai Yang, David Gersten, and Di Yan. A real time dose monitoring and dose reconstruction tool for patient specific vmat qa and delivery. *Medical Physics*, 39(12):7194–7204, 2012. doi: <http://dx.doi.org/10.1118/1.4764482>. URL <http://scitation.aip.org/content/aapm/journal/medphys/39/12/10.1118/1.4764482>.

- [33] Juan F. Calvo-Ortega, Tony Teke, Sandra Moragues, Miquel Pozo, and Joan Casals. A varian dynalog file-based procedure for patient dose-volume histogram-based imrt qa. *Journal of Applied Clinical Medical Physics*, 15(2): 100–109, 2014. URL <http://www.ncbi.nlm.nih.gov/pubmed/24710455>.
- [34] Jianguo Qian, Louis Lee, Wu Liu, Karen Chu, Edwark Mok, Gary Luxton, Quynh-Thu Le, and Lei Xing. Dose reconstruction for volumetric modulated arc therapy (vmat) using cone-beam ct and dynamic log files. *Physics in Medicine and Biology*, 55:3597–3610, 2010. URL <http://iopscience.iop.org/0031-9155/55/13/002/>.
- [35] Baozhou Sun, Dharanipathy Rangaraj, Sunita Boddu, Murty Goddu, Deshan Yang, Geethpriya Palaniswaamy, Sridhar Yaddanapudi, Omar Wooten, and Sasa Mutic. Evaluation of the efficiency and effectiveness of independent dose calculation followed by machine log file analysis against conventional measurement based imrt qa. *Journal of Applied Clinical Medical Physics*, 13(5), 2012. ISSN 15269914. URL <http://www.jacmp.org/index.php/jacmp/article/view/3837>.
- [36] Dewayne L. Defoor, Luis A. Vazquez-Quino, Panayiotis Mavroidis, Nikos Papanikolaou, and Sotirios Stathakis. Anatomy-based, patient-specific vmat qa using epid or mlc log files. *Journal of Applied Clinical Medical Physics*, 16(3): 206–215, 2015.
- [37] Marlies Pasler, Jochem Kaas, Thijs Perik, Job Geuze, Ralf Dreindl, Thomas Künzler, Frits Wittkamper, and Dietmar Georg. Linking log files with dosimetric accuracy - a multi-institutional study on quality assurance of volumetric modulated arc therapy. *Radiotherapy and Oncology*, 117(3):407–411, December 2015. URL <http://dx.doi.org/10.1016/j.radonc.2015.11.005>.
- [38] Tobias Eckhause, Hania Al-Hallaq, Timothy Ritter, John DeMarco, Karl Farrey, Todd Pawlicki, Gwe-Ya Kim, Richard Popple, Vijeshwar Sharma, Mario Perez, SungYong Park, Jeremy T. Booth, Ryan Thorwarth, and Jean M. Moran. Automating linear accelerator quality assurance. *Medical Physics*, 42(10):6074–6083, October 2015. URL <http://dx.doi.org/10.1118/1.4931415>.
- [39] C Kabat, D Defoor, A Alexandrian, N Papanikolaou, and S Stathakis. Su-f-t-233: Evaluation of treatment delivery parameters using high resolution elekta log files. *Medical Physics*, 43(6):3515–3516, 2016. ISSN 2473-4209. doi: 10.1118/1.4956372. URL <http://dx.doi.org/10.1118/1.4956372>.

- [40] C Stanhope, J Liang, D Drake, and D Yan. Th-ab-201-12: Using machine log-files for treatment planning and delivery qa. *Medical Physics*, 43(6):3852–3852, 2016. ISSN 2473-4209. doi: 10.1118/1.4958041. URL <http://dx.doi.org/10.1118/1.4958041>.
- [41] Pejman Rowshanfarzad, Conor McGarry, Michael Barnes, Mahsheed Sabet, and Martin Ebert. An epid-based method for comprehensive verification of gantry, epid and the mlc carriage positional accuracy in varian linacs during arc treatments. *Radiation Oncology*, 9(1):249, 2014. ISSN 1748-717X. doi: 10.1186/s13014-014-0249-8. URL <http://www.ro-journal.com/content/9/1/249>.
- [42] Mitsuhiro Inoue, Hiroya Shiomi, Kengo Sato, Junichi Taguchi, Kohei Okawa, Kosaku Inada, Taro Murai, Izumi Koike, Koshi Tatewaki, Seiji Ota, and Tomio Inoue. Effect of residual patient motion on dose distribution during image-guided robotic radiosurgery for skull tracking based on log file analysis. *Japanese Journal of Radiology*, 32:461–466, May 2014. <http://link.springer.com/article/10.1007%2Fs11604-014-0330-0>.
- [43] Lydia L. Handsfield, Ryan Jones, David D. Wilson, Jeffrey V. Siebers, Paul W. Read, and Quan Chen. Phantomless patient-specific tomotherapy qa via delivery performance monitoring and a secondary monte carlo dose calculation. *Medical Physics*, 41(10):101703, October 2014. <http://dx.doi.org/10.1118/1.4894721>.
- [44] Nathan Childress, Quan Chen, and Yi Rong. Parallel/opposed: Imrt qa using treatment log files is superior to conventional measurement-based method. *Journal of Applied Clinical Medical Physics*, 16(1), 2015. http://www.jacmp.org/index.php/jacmp/article/view/5385/html_202.
- [45] Heng Li, Narayan Sahoo, Falk Poenisch, Kazumichi Suzuki, Yupeng Li, Xiaoliang Li, and Xiaodong Zhang. Use of treatment log files in spot scanning proton therapy as part of patient-specific quality assurance. *Medical Physics*, 40(2):021703, February 2013. URL <https://www.ncbi.nlm.nih.gov/pmc/articles/PMC3555925/>.
- [46] X. Ronald. Zhu, Yupeng Li, Dennis Mackin, Heng Li, Falk Poenisch, Andrew K. Lee, Anita Mahajan, Steven J. Frank, Michael T. Gillin, Narayan Sahoo, and Xiaodong Zhang. Towards effective and efficient patient-specific quality assurance for spot scanning proton therapy. *Cancers*, 7:631–647, 2015. URL <https://www.ncbi.nlm.nih.gov/pmc/articles/PMC4491675/>.

- [47] D Scandurra, F Albertini, R van der Meer, G Meier, D C Weber, A Bolsi, and A Lomax. Assessing the quality of proton pbs treatment delivery using machine log files: comprehensive analysis of clinical treatments delivered at psi gantry 2. *Physics in Medicine and Biology*, 61(3):1171, 2016. URL <http://stacks.iop.org/0031-9155/61/i=3/a=1171>.
- [48] Clinic set to maximize clinical availability and performance with elekta intellimax. <http://www.waymaker.net/bitonline/2004/08/02/20040802BIT20510/wkr0001.pdf>. Elekta AB, accessed February 2016.
- [49] Linacwatch. <http://www.qualiformed.com/linacwatch?tid=2>. Quali-formed SARL, accessed March 2016.
- [50] *Agility und Integrity R3.1 - Gebrauchsanweisung - Klinischer Modus*. Elekta AB, Stockholm, Sweden, 2013. German.
- [51] *Elekta Medical Linear Accelerator - Instructions for Use Supplement - Clinical Mode*. Elekta AB, Stockholm, Sweden, 2014.
- [52] *User Manual Delta-4 Phantom*. ScandiDos AB, Uppsala, Sweden. D001 32 002 01.
- [53] Scandidos delta-4 phantom, schematic. <http://conmedica.com/wp-content/uploads/2014/09/Delta4-IMRT-Qualitaetssicherung.jpg>. Conmedica High End Radiotherapy, accessed July 2015.
- [54] Daniel A. Low, William B. Harms, Sasa Mutic, and James A. Purdy. A technique for the quantitative evaluation of dose distributions. *Medical Physics*, 25(5):656–661, May 1998. URL http://personal.us.es/alberto/ffisim/material/gamma_index.pdf.
- [55] Rudolf Frühwirth. *Wahrscheinlichkeitsrechnung und Statistik für Studierende der Physik*. Rudolf Frühwirth & bookboon.com, 1st edition, 2015. ISBN 978-87-403-0847-1. German.